THE ASTROPHYSICAL JOURNAL, 310:621–636, 1986 November 15

THE GLOBAL SPIRAL STRUCTURE OF M81: RADIO CONTINUUM MAPS

FRANK N. BASH
Department of Astronomy, The University of Texas at Austin
AND
MICHELE KAUFMAN
Department of Physics, The Ohio State University
Received 1986 February 24; accepted 1986 April 24

ABSTRACT

VLA observations of the radio continuum emission from M81 at wavelengths of 6 and 20 cm are presented and used to check the predictions of density-wave theories. Both extended nonthermal radiation and giant radio H II regions are detected on a series of maps that range in resolution from 10″ to 18″. The nonthermal radio emission defines spiral arms that are patchy and well-resolved, with a width of 1–2 kpc. The observed nonthermal arms are too broad to agree with Visser's hydrodynamic model for a classical density wave in M81 unless the scale height of the shocked layer is 4–8 times the scale height adopted by Visser for the H I disk. The observed arm widths seem to agree better with the predictions of a density-wave model that emphasizes the clumpy nature of the interstellar medium; for example, the cloudy density-wave model of Roberts and Hausman.

Along the spiral arms, only a few small patches have peak polarized intensity above the 3 σ level. For a typical nonthermal emission peak along the arms, our upper limits on the degree of linear polarization are 18%–27% at 20 cm and 28%–38% near the southern major axis at 6 cm. The 20 cm arms spiral outward from a faint inner H I ring. This might suggest that the H I ring is produced by the inner Lindblad resonance and thus places the ILR farther from the center of M81 than assumed in Visser's models.

The pitch angles of the radio continuum arms are estimated; the two main spiral arms differ in pitch angles. Major distortions with respect to a logarithmic spiral seem to occur where the concentration of giant radio H II regions is greatest and in the north, where tidal effects by M82 may have been important.

Subject headings: galaxies: individual — galaxies: structure — nebulae: H II regions — polarization — radio sources: galaxies

I. INTRODUCTION

Although more than 20 yr have passed since Lin and Shu (1964) proposed their density wave theory to account for spiral structure in grand design galaxies, this theory still provokes considerable interest and debate. As a test of density wave theories, we are making a comprehensive observational study of the spiral arms in M81.

An easily-resolved spiral galaxy with a global two-armed pattern and an inclination of 59° suitable for dynamical studies, M81 is a prime candidate for testing density-wave theories. Certain previous studies support a density-wave interpretation for this galaxy. Visser (1978, 1980) finds very strong evidence for a nonlinear density wave in the H I gas in M81, while the broad-band surface photometry of Schweizer (1976), Elmegreen (1981), and Elmegreen and Elmegreen (1983) reveals a stellar density wave in the old disk stars. The stellar density wave is clearly seen in Elmegreen's *I* band photograph. Using Visser's hydrodynamic model for the gas in M81 and the Ballistic Particle model of Bash and Peters (1976) for the molecular clouds, Bash and Visser (1981) and Leisawitz and Bash (1982) predict the spatial distribution and radial velocities of giant H II regions and young stars in M81. The resulting distribution of young stars resembles an optical photograph of M81.

As part of this investigation of spiral structure we have used the VLA (Very Large Array)[1] to make radio continuum observations of M81 at wavelengths of 6 and 20 cm. In this first of a series of papers on our radio observations of M81, we present radio continuum maps suitable for studying the spiral arms, and we use these to compare the radio continuum data alone with predictions of various density-wave models. In Kaufman *et al.* (1986*a*, hereafter Paper II), we shall see how well the spiral arms defined by various spiral tracers in M81 correspond with one another and with the predictions of density-wave theories. In particular we shall compare the locations and pitch angles of spiral arms seen in young stars (Hα, *B* light, and $B-I$ color), in the radio continuum, in old stars (*I* band), in the H I intensity data, and in the H I velocity residual data (velocity shock).

Density-wave theories predict a compression zone along the inside edge of the spiral arms, where a two-armed spiral-shock would compress interstellar gas and magnetic fields. In hydrodynamic calculations, where the gas is treated as a continuous single-component medium, the width of the shock layer is small, typically 50 pc (see Roberts 1969; Shu *et al.* 1972). Since M81 is not seen face-on, the width of the nonthermal emission ridge in the plane of the sky would exceed this value and would

[1] The National Radio Astronomy Observatory is operated by Associated Universities, Inc., under contract with the National Science Foundation.

TABLE 1

VLA OBSERVATIONS AT 6 AND 20 CENTIMETERS

DATE	ARRAY	FIELD	ν (GHz)	N	t (hr)	Δt (s)	$\Delta\nu$ (MHz)	PHASE CENTER α(1950.0)	PHASE CENTER δ(1950.0)	S_ν(nuc) (mJy)
1981 Aug 14	B	M81	1.413	27	12	20	25	$9^h51^m27^s.340$	69°18′08″.20	53.3 ± 0.5
1981 Aug 16	B	M81	4.873	27	13	20	25	9 51 27.340	69 18 08.20	89.5 ± 0.9
1982 Nov 6	D	M81-S	4.885	27	8	20	50	9 51 44.700	69 16 22.00	90.7 ± 0.9
1983 Jan 26	C	M81	1.465	24	9.5	30	50	9 51 27.340	69 18 08.20	69.0 ± 0.7
1983 Jan 28	C	M81-N	4.885	26	7	30	50	9 51 00.000	69 20 00.00	69.2 ± 0.7
	C	M81-S	4.885	26	4	30	50	9 51 44.700	69 16 22.00	72.8 ± 0.7
1983 Jan 29	C	M81-S	4.885	21	3	30	50	9 51 44.700	69 16 22.00	

depend on the scale height of the shocked layer that emits the synchrotron radiation. The relevant layer is probably the, as yet undetected, molecular gas. If, as in our Galaxy, the scale height of molecular hydrogen is one-half that of atomic hydrogen and if we adopt Visser's values of 200–300 pc for the thickness of the H I disk (full width half-density) in M81, then we predict a shock width of 100–140 pc in the plane of the sky. Alternatively, if the relevant shocked layer were the H I gas, then we would predict a width of 180–260 pc in the plane of the sky.

Roberts and Hausman (1984) propose an alternative density-wave model. They postulate a spiral gravitational perturbation but do an N-body calculation to simulate a cloudy interstellar medium. Their model produces a spiral density enhancement about 1 kpc wide and a spiral "shock front" 300–600 pc in width, significantly broader than the 50 pc width predicted by continuum gasdynamical models. Whereas their calculations are for a model with parameters appropriate to our Galaxy, we expect qualitatively similar results for M81.

To look for the expected nonthermal emission ridge predicted by either the hydrodynamic or the cloudy version of a spiral density wave, we have taken "scaled-array" data at 6 and 20 cm and constructed a set of maps in which the diameter θ of the synthesized half-power beam varies from 4″ to 18″. Since the distance of M81 is estimated to be 3.3 ± 0.6 Mpc (Bottinelli *et al.*, 1984) or 4.0 ± 0.4 Mpc (de Vaucouleurs 1981) or 5.75 Mpc (Sandage 1984), 10″ corresponds to 160–280 pc along the major axis and 310–540 pc along the minor axis. Thus we can determine whether the width of the radio continuum arms fits the predictions of either the hydrodynamic or the cloudy version of a spiral density-wave model.

The radio continuum arms in M81, which is an Sab spiral, are much fainter than in the Sc galaxy M51, where the nonthermal emission ridge appears clearly in the Westerbork data (Mathewson, Kruit, and van der Brouw 1972; Segalovitz 1976). Using the WRST, Segalovitz (1977) has made 20 cm maps of the nonthermal disk emission from M81. His global map with highest resolution has a synthesized half-power beam of 24″ × 26″ and shows some individual radio peaks along the optical arms. Whereas the general disk emission from M81 is too extended to be detected by the VLA, our higher resolution, lower noise data gives a better radio picture of the spiral arms. If the compression zone along the spiral arms were as narrow as predicted by the hydrodynamic density-wave model, then the radio emission from this zone would be easier to detect in our VLA data than in the lower resolution WRST data. In fact, we shall find that the nonthermal emission along the arms is clearly resolved on our maps and is appreciably broader than one would expect from a hydrodynamic calculation for a single component medium and the above estimates of layer smearing.

II. OBSERVATIONS AND DATA REDUCTION

Table 1 lists the observing dates and VLA configurations and values for the frequency, the number of antennas N, the duration of observations t, the bandwidth $\Delta\nu$, the averaging time Δt, and the coordinates of the phase center for our VLA observations at 6 and 20 cm. At 20 cm the primary half-power beam is larger than the galaxy, and we selected the compact source in the nucleus as the phase center. At 6 cm, the 9′ primary half-power beamwidth is smaller than the main body of M81 which extends about 20′ along the major axis. To map the spiral arms at 6 cm, we chose to observe two fields: one, which we call M81-N, is centered 3.′05 northwest and the other, which we call M81-S, is centered 2.′34 southeast of the nucleus.

The phase calibration source 0836+710 was observed at 30 minute intervals. The gain calibration is based on the source 3C 286, and the polarization calibration, on 3C 286, 3C 138, and 0836+710. The flux density values assumed for 3C 286 were 14.51 Jy at 1.465 GHz and 7.410 Jy at 4.885 GHz. The resulting values for the flux density of 0836+710 at 4.885 GHz are given in Table 2. The three measurements at this frequency indicate a 1% random error in the calibration solution.

We used the standard AIPS (Astronomical Image Processing System) reduction programs to edit, Fourier transform, and self-calibrate the (u, v) data and to "clean" the resulting maps. At 20 cm it was necessary to clean an area of at least 27′ × 27′ so as to include within the cleaned region the two relatively strong background sources labeled 1 and 124 in Figure 1 (and listed as sources 1 and 2 in Emerson, Kronberg, and Wielebinski 1978). The cleaned area for each of the total intensity 20 cm maps in the figures below is at least as large as the region displayed in Figure 1. Smaller maps were produced at 6 cm since here primary beam attenuation dominates the effects of confusion by distant sources. At both frequencies the total intensity maps were made with estimates for the zero-spacing flux weighted by the VLA primary beam. For the zero-

TABLE 2

FLUX DENSITY OF PHASE CALIBRATION SOURCE 0836+710

Date	ν (GHz)	S_ν (Jy)
1982 Nov 6	4.885	2.672 ± 0.009
1983 Jan 28	4.885	2.725 ± 0.005
1983 Jan 29	4.885	2.700 ± 0.006

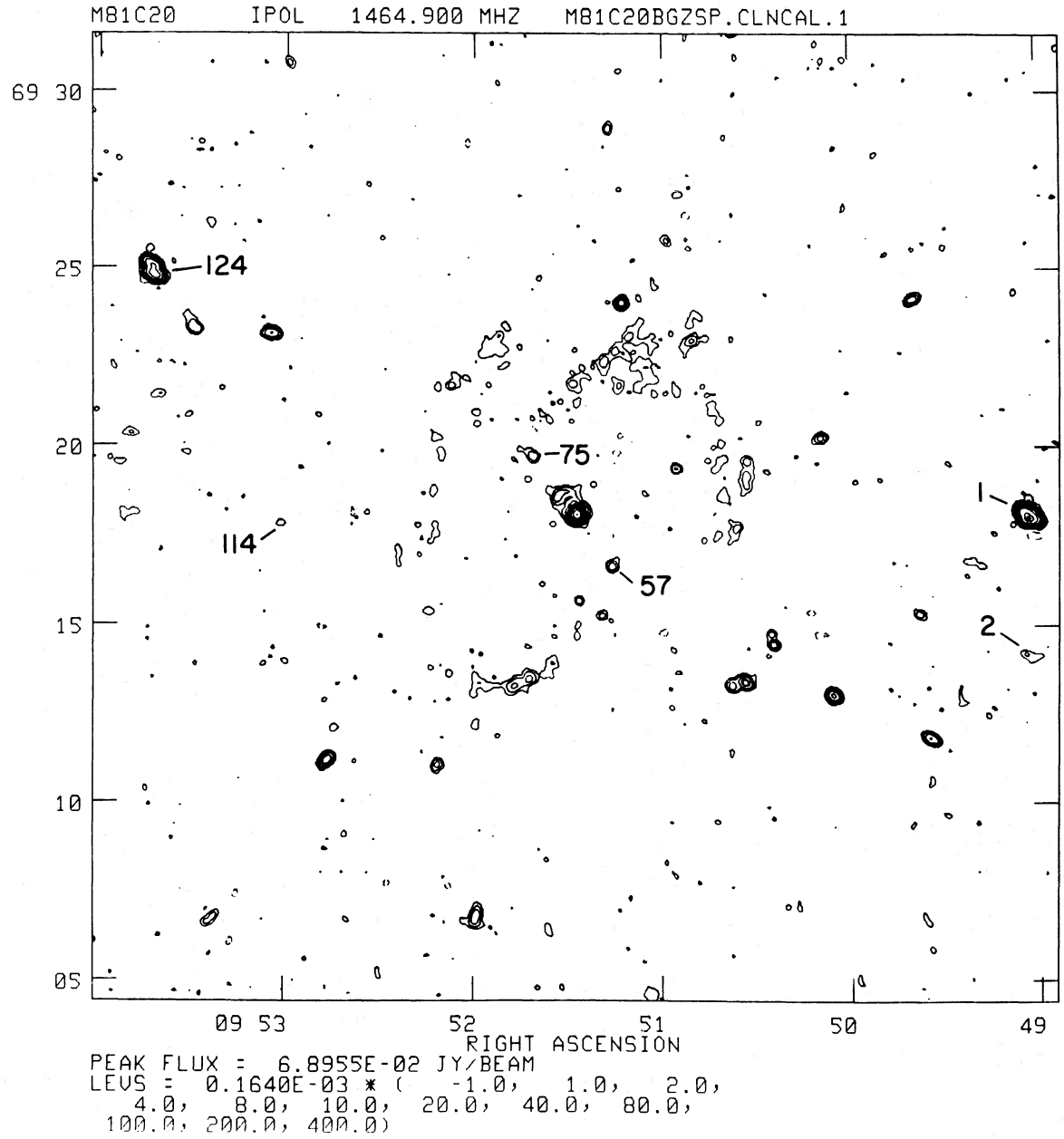

FIG. 1.—A large field plot of the 20 cm emission from the cleaned region of the total-intensity map designated number 1 in Table 3. The solid contour levels are at 3 σ, 6 σ, 12 σ, 24 σ, 30 σ, 60 σ, 120 σ, 240 σ, ..., 1200 σ, and the dashed contour level is at -3 σ. The phase center is the bright compact source in the nucleus. Numbered features are discussed in the text.

spacing flux at 6 cm we used Beck's (1983) observations with the 100 m telescope at MPIfR, while for the zero-spacing flux at 20 cm, we extrapolated from 100 m observations at 11 cm (Emerson, Kronberg, and Wielebinski 1978) and 6 cm. After cleaning, any excess flux density was subtracted to give a mean intensity $I = 0$ in source-free regions outside of M81.

For the maps of linearly polarized intensity, one needs to correct for the positive bias that results from rms noise in the Q and U Stokes parameters. That is, in the absence of any signal, Q and U are Gaussian-distributed random variables with zero mean. The polarized intensity, $I_{\rm pol} \equiv (Q^2 + U^2)^{1/2}$, does not have a Gaussian distribution or a zero mean. To correct for the nonzero mean, we measured the mean polarized intensity in large source-free regions of the map and then subtracted this mean value from each polarized intensity value in the map.

From the sets of data listed in Table 1, we have made various maps with a synthesized half-power beam width θ ranging in size from 1″ (for our highest resolution data at 6 cm) to 18″. For convenience we take the distance of M81 as 4 Mpc. Then 1″ equals 19 pc along the major axis and 37 pc along the minor axis. Better information about the distance of M81 can be used to scale our values for linear dimensions accordingly. The higher resolution maps do not show the spiral arms clearly and will be used in a later paper to study the nucleus of M81. The results here on the global spiral structure are derived primarily from our lower resolution maps with $\theta \geq 10''$. Table 3 specifies

TABLE 3

RADIO CONTINUUM MAPS OF THE GLOBAL SPIRAL STRUCTURE OF M81

MAP	FIELD	λ (cm)	ARRAY	BEAM	CELL	σ I (μJy/Ω_B)	σ T_b (K)	FIGURES WHERE USED
A. Total Intensity Maps								
1	M81	20.5	C	12".7 × 12".4	3".2	55	0.20	1
2	M81	20.5	B, C	10.0 × 10.0	1.9	48	0.28	2, 9, 10
3	M81	20.5	B, C	12.0 × 12.0	1.9	54	0.21	3, 14
4	M81	20.5	C	17.0 × 17.0	3.2	72	0.14	4
5	M81-S	6.1	D	12.0 × 12.0	2.7	37	0.013	5
6	M81-S	6.1	C, D	18.2 × 17.8	4.5	37	0.0059	6, 7*b*
7	M81-S	6.1	C, D	15.0 × 15.0	1.9	29	0.0066	7*a*
8	M81	20.5	B, C	15.0 × 15.0	1.9	71	0.18	7*a*, 15, 16
9	M81-N	6.1	C	10.0 × 10.0	1.9	47	0.024	8, 9, 10
10	M81-S	6.1	C, D	10.0 × 10.0	1.9	25	0.013	8, 9
11	M81	20.5	B, C	9.7 × 9.2	1.9	44	0.28	11, 12
12	M81	20.5	C	17.2 × 17.4	4.0	72	0.14	13
13	M81	20.5	B, C	18.2 × 18.2	1.9	89	0.15	7*b*
B. Maps of Linearly Polarized Intensity								
1P	M81	20.5	C	12.7 × 12.4	3.2	29	0.106	...
2P	M81	20.5	C	17.2 × 17.4	4.0	26	0.050	...
3P	M81-S	6.1	D	11.3 × 10.3	2.7	30	0.013	...
4P	M81-S	6.1	D	18.8 × 18.4	4.5	24	0.0036	...
5P	M81-S	6.1	C, D	17.8 × 18.2	4.5	19	0.0030	...

the values of the map parameters for the figures in this paper: the half-power diameters of the synthesized Gaussian beam, the width of a square pixel, and the rms noise σ measured on the map. The noise in the intensity values is listed in units of μJy/Ω_B, where Ω_B is the synthesized beam area.

Some of our maps result from data taken with a single VLA configuration, while others result from combining observations taken with two different configurations. For the latter maps, we subtracted the nucleus region before combining the data since the compact source in the nucleus is variable. This variation in the flux density S_ν(nuc) of the compact source is shown in Table 1, where we list the values of S_ν(nuc) measured on the highest resolution map made from each data set. The uncertainties given here are 1% of the peak values, as determined by the random error in the calibration solution. For the compact source in the nucleus the calibration errors dominate the rms noise σ since on these maps the values of S_ν(nuc)/σ range from 9×10^2 to 2.5×10^3.

The fact that we have data at two different wavelengths (6 and 20 cm) and three different VLA configurations allows us to compute spectral index values for the brighter portions of the spiral arms and the central source. These spectral maps use "scaled array" pairs, e.g., the D configuration of the VLA at 6 cm plus the C configuration of the VLA at 20 cm. For each scaled array pair the more compact array samples approximately the same spatial frequencies (antenna spacing divided by wavelength) at 6 cm as the other array does at 20 cm.

After the data were obtained, we experimented with weighting the (u, v) data with various tapering functions. Tapering reduces the sidelobes of the synthesized beam, increases the noise in the map, and increases the width of the synthesized beam. In the resulting set of 6 cm maps, the rms noise σ increases less rapidly than the beam size θ; so by increasing the width of the synthesized beam, we increase the sensitivity to linear features such as a nonthermal emission ridge along the spiral arms. The expected nonthermal ridge would emit a greater intensity at 20 cm. At 20 cm our maps are confusion limited. For the set of 20 cm maps made by combining data from B and C arrays, we find that the value of σ/θ first decreases by a factor of 2.5 as θ increases from 4" to 9".5 but then remains nearly constant as θ increases from 9".5 to 18". Therefore at 20 cm, increasing the beamwidth beyond 9".5 does not increase the sensitivity to a *narrow* spiral arm compression ridge.

III. DETECTION OF THE RADIO CONTINUUM ARMS OF M81

We detect the spiral arms of M81 in the radio continuum. In Figures 1, 2, 3, 4, 5 and 6 the total intensity is displayed without correction for primary beam attenuation, and thus the noise is nearly uniform across the plot. The spectral index plots of Figures 7 and 10 and the face-on picture in Figure 15 show maps corrected for primary beam attenuation.

a) The 20 Centimeter Maps

Figure 1 is a large field contour plot made from the C array data at 20 cm with a synthesized beam of 12".7 × 12".4. It shows the emission from the spiral arms and the bright source in the nucleus. To indicate the flux scale we note that source number 57, an unresolved source near the central part of M81, has $S_\nu(20\text{ cm}) = 1.07 \pm 0.07$ mJy. If Cas A were at the 4 Mpc distance adopted for M81, it would be a 1.7 mJy source. This figure also shows the presence of several relatively strong background sources in the environs of M81. These will be discussed further in § V, where we shall argue that, at most, only a few of the brighter sources along the spiral arms are likely to be chance coincidences with background sources.

The 20 cm maps displayed in Figures 2 (Plate 6) and 3 result from combining data taken with B and C arrays after removal of the bright source in the nucleus. For Figure 2 the synthesized beam is 10" × 10"; for the contour plot in Figure 3 the synthesized beam is 12" × 12". Extended emission along

PLATE 6

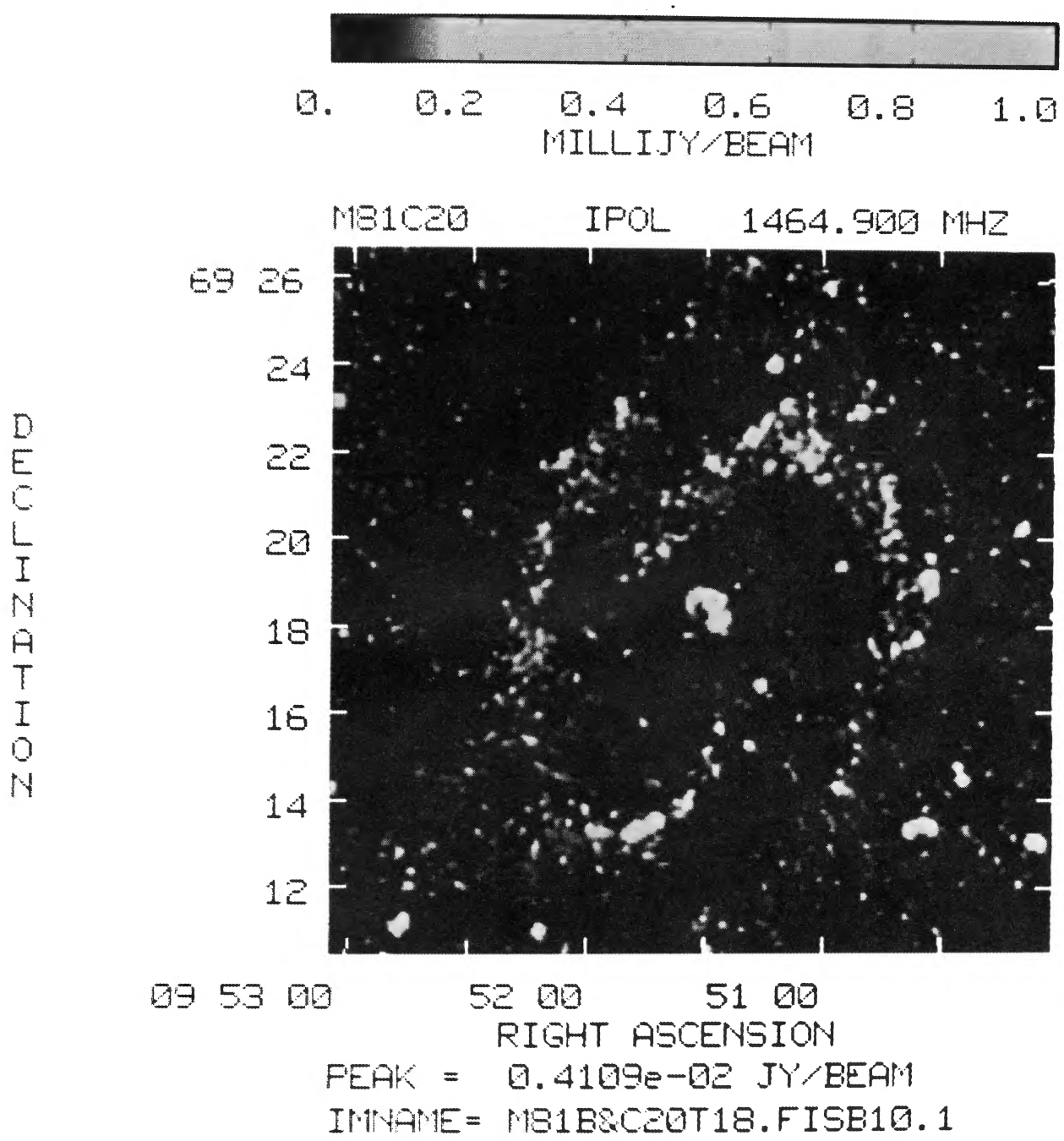

FIG. 2.—A portion of map 2 showing the 20 cm emission from the spiral arms of M81 with a resolution of 10″ × 10″. The bright variable source in the nucleus was removed from the data before making this map.

BASH AND KAUFMAN (*see* page 624)

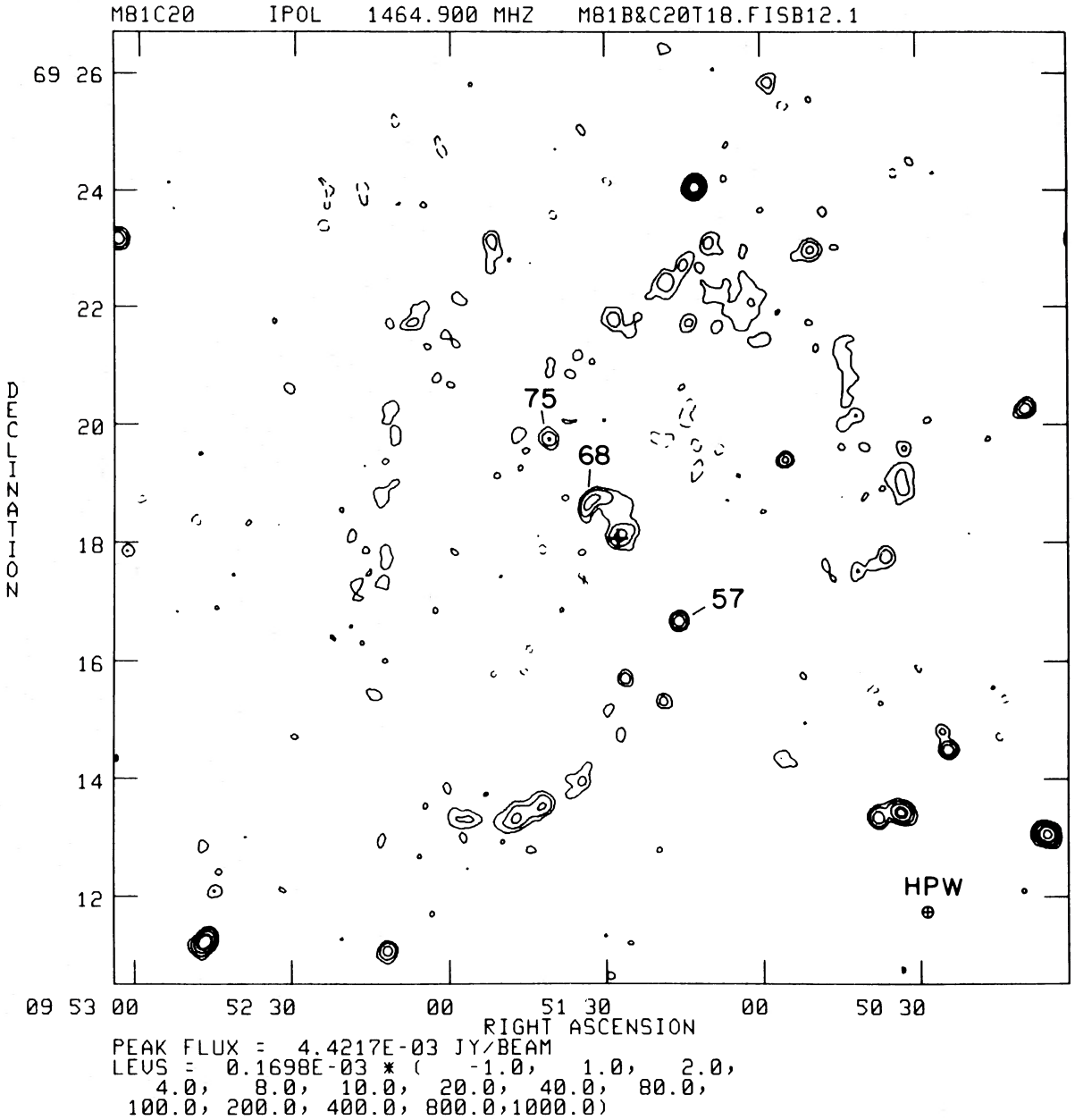

FIG. 3.—A portion of map 3 showing the 20 cm emission with a resolution of 12″ × 12″. The solid contour levels are at 3.1 σ, 6.2 σ, 12.4 σ, 24.8 σ, 31 σ, 62 σ, 124 σ, . . . , and the dashed contour level is at -3.1 σ. The bright compact source in the nucleus was subtracted from the data at the location of the plus sign. The numbered sources tend to give a barlike or jetlike appearance to the central region of M81.

the spiral arms is visible on the map in Figure 2 but not on maps with appreciably higher resolution. With a few exceptions, the brighter individual features along with the arms are thermal sources and, as we shall see in Paper II, coincide with H II regions. About half of these thermal radio sources have peak brightness temperature T_b greater than 1.6 K. A map with a resolution of 100 pc shows some of these giant H II regions, but not the more extended emission. Among our series of 20 cm maps, the map shown in Figure 2 is the one most sensitive to linear features with width less than 200 pc, that is, to the narrow linear features predicted by a hydrodynamic density-wave calculation.

Figure 4 (Plate 7) shows a lower resolution 20 cm map that is twice as sensitive as the map in Figure 2 to features broader than 340 pc. This map does a better job of revealing the faint outer extensions of the arms. In particular, the very northern part of the eastern arm gives indications of the same splitting that is visible in the H I maps made by Rots and Shane (1975). Figures 2 and 4 may give the impression that M81 is a barred spiral. We have looked at short-exposure plates of M81 in the Kitt Peak 4 m plate collection and see no optical evidence for a bar. The "barlike" appearance of our 20 cm maps is largely the result of (1) two discrete sources (numbered 57 and 75 in Fig. 1) that line up with the compact source in the nucleus near the inner endpoints of the 20 cm arms, and (2) a kpc-sized feature (source number 68) that is just northeast of the compact source and lies roughly along the same line. Sources 57 and 75 may form a double-lobed radio source powered by jets from the

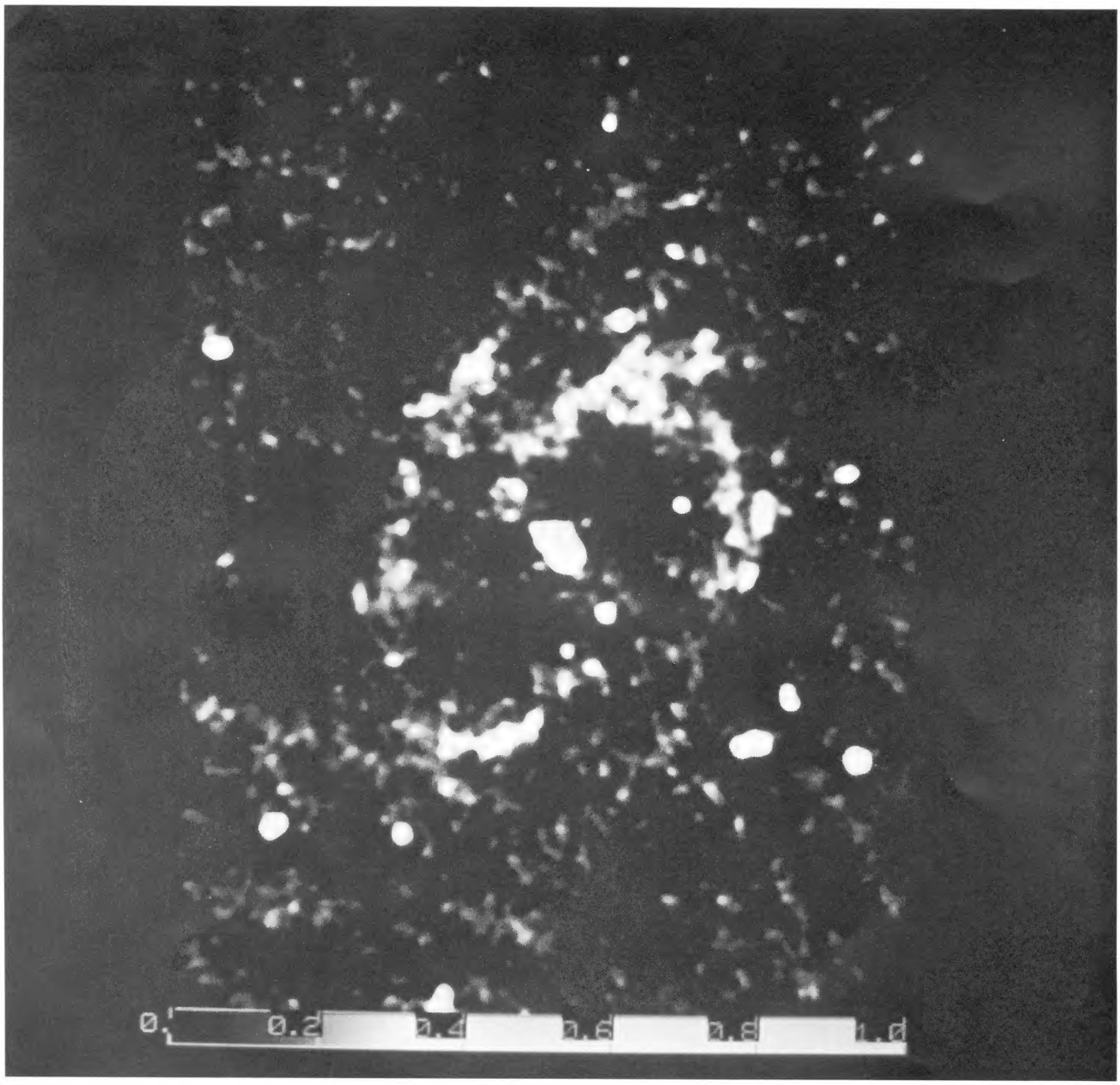

FIG. 4.—A lower resolution map (map 4) of the 20 cm emission from M81

BASH AND KAUFMAN (*see* page 625)

central source. We shall discuss this further in a separate paper on the nucleus of M81.

The small-scale spikiness of the extended emission along the arms (see Figs. 2 and 4) is an artifact of the CLEAN program used in the reductions. However, the extended emission also appears clumped along the arms on scales in excess of several beamwidths, and this patchy quality is probably real. In § III*b* we shall determine whether the extended emission along the arms is thermal or nonthermal, and in § IV we shall measure the arm widths at positions that avoid the giant H II regions. Thus we shall test whether this extended emission fits the expected compression from a hydrodynamic density-wave model.

b) The 6 Centimeter and Spectral Index Maps

In Figures 5 and 6 we show contour plots of the 6 cm emission from the field M81-S. Figure 5, which is based on the D array data alone, shows the nucleus, the two sources (numbers 57 and 75) that lie on a line through the nucleus, and some individual sources along the eastern arm of the galaxy. This map has the same (12″ × 12″) resolution as the 20 cm map in Figure 3. The eastern arm is more evident in the more sensitive, lower resolution map of Figure 6, which is constructed from C and D array data after the bright nucleus was subtracted from the (*u*, *v*) data.

Figure 6 also reveals a string of radio sources heading south

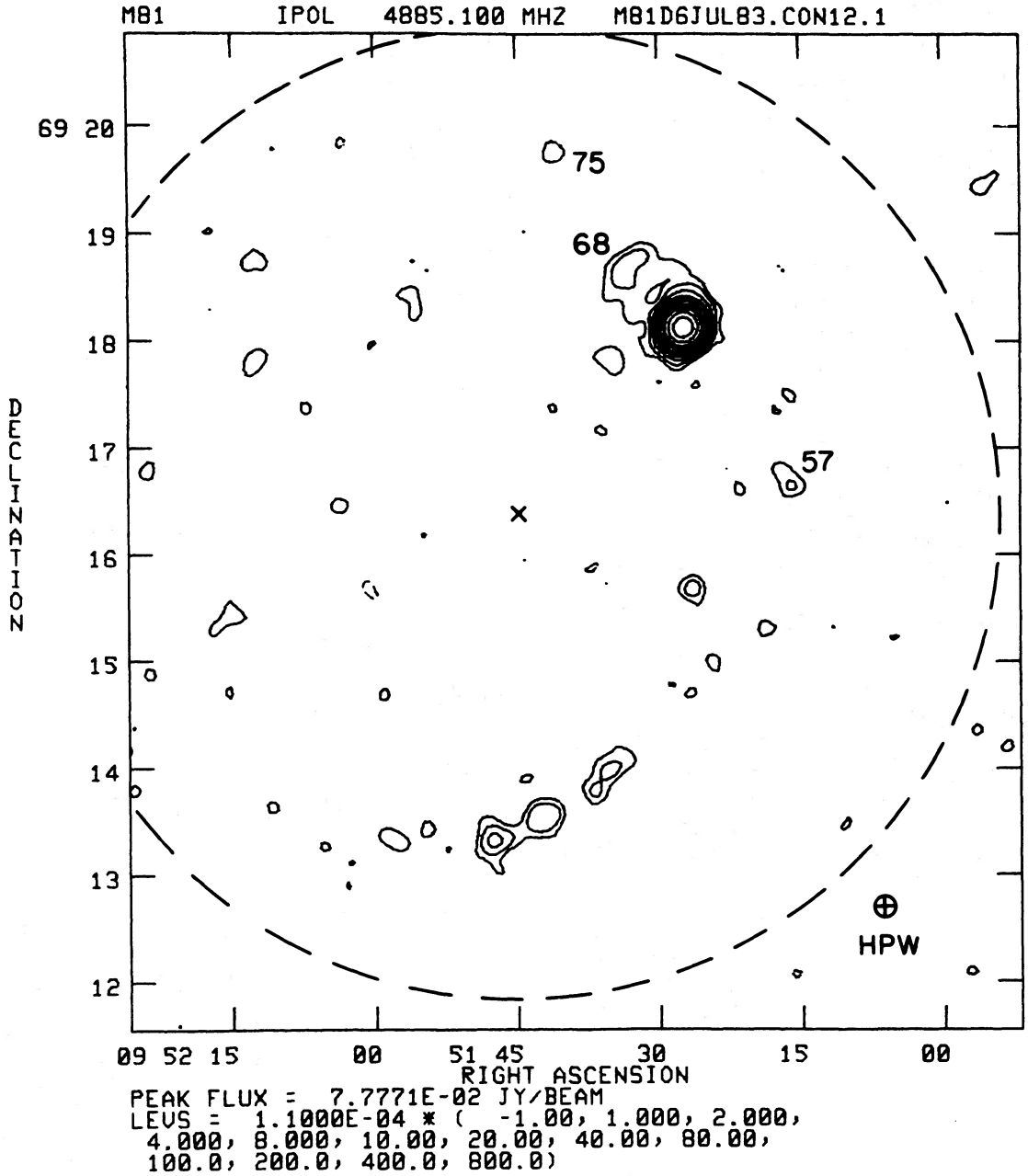

FIG. 5.—A plot of map 5, which shows the 6 cm emission from the field M81-S with a resolution of 12″ × 12″. The position of the phase center is marked by an X and that of the primary half-power beam, by a dashed circle. The solid contour levels are at 3 σ, 6 σ, 12 σ, ..., 2400 σ, and the dashed contour level is at -3σ.

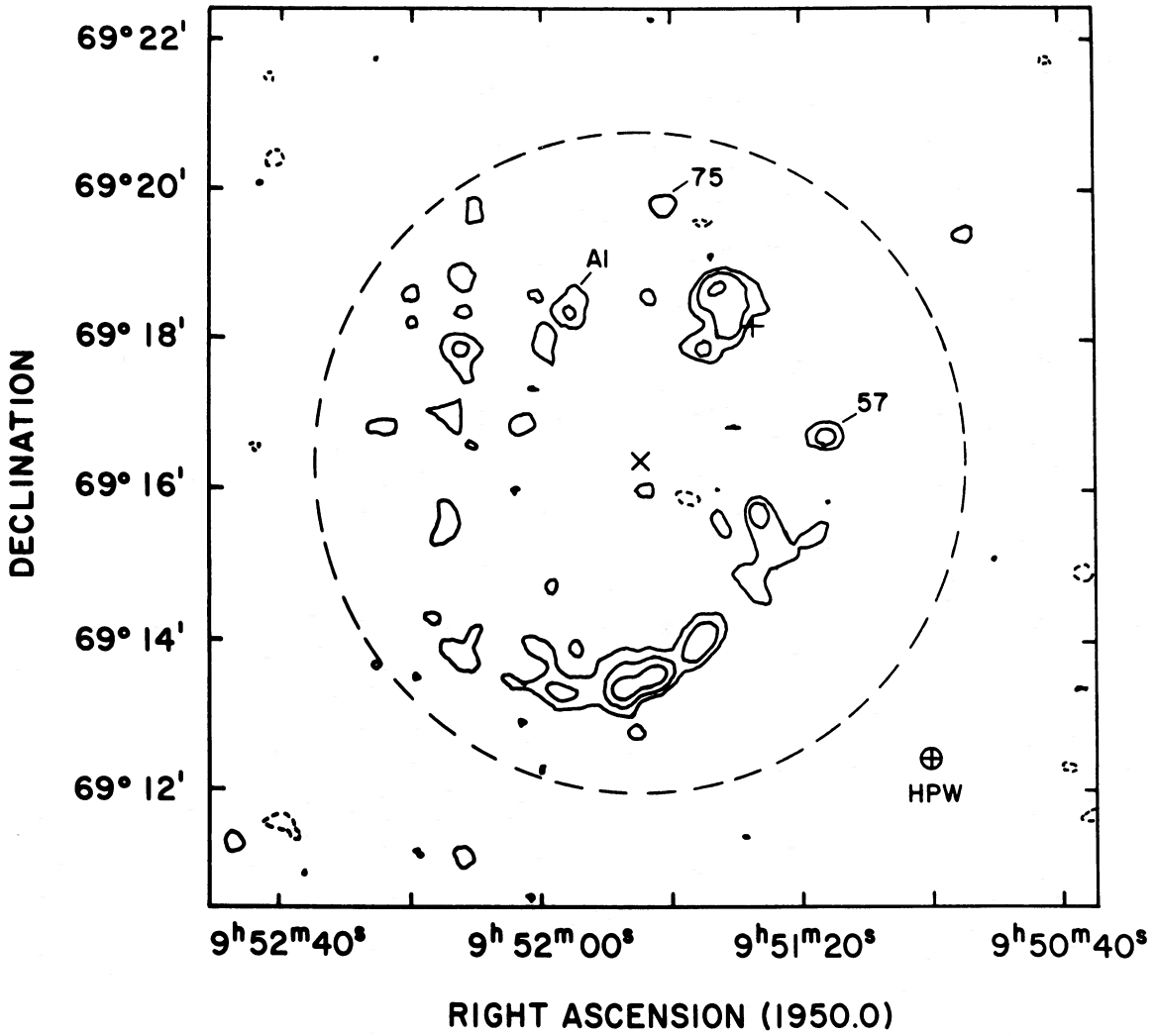

FIG. 6.—A lower resolution map (map 6) of the 6 cm emission from the field M81-S. The position of the phase center is marked by an X and the location of the primary half-power beam, by a dashed circle. The bright compact source in the nucleus was subtracted from the data at the location of the plus sign. The solid contour levels are at 3 σ, 6 σ, and 12 σ, and the dashed contour level is at -3 σ. This map shows the eastern arm and a string of sources (heading south from source A1) along the inner H I ring.

from the source numbered A1 and lying along what seems to be a faint inner extension of the western 20 cm arm. In Paper II we shall see that this inner southern extension of the western arm coincides with part of a faint H I ring. The ring is visible in the H I maps of M81 made by Hine and Rots (1986) at the VLA and displayed in Hine (1984). When deprojected into the plane of M81, the H I ring has a radius of $4'.3 \pm 0'.2$, and the 20 cm arms appear to spiral outwards from this ring. Rots (1975) notes the presence of the H I ring in his lower resolution WRST data. He suggests that it may be related to the inner Lindblad resonance (ILR) but cautions that the ringlike appearance may be an artifact of projection and the low resolution of the WRST. Our data show that the 20 cm arms end at the H I ring. This favors the interpretation that the H I ring is the ILR. This viewpoint will be discussed further in Paper II when we consider the radial distribution of giant radio H II regions. We note that the ring has a larger radius than the $2'.6$ radius adopted by Visser (1980) for the ILR.

To make a spectral index map of the M81-S field, we used a 6 cm map derived from the C and D array data and a 20 cm map derived from the B and C array data. We interpolated the 6 cm map so that both maps are on the same coordinate grid as the map in Figure 2 and then convolved both to a $15'' \times 15''$ beam. For the resulting spectral index map, shown in Figure 7*a* (Plate 8), we restrict to values of the intensity $I_\nu(20\text{ cm}) \geq 2\ \sigma$ and $I_\nu(6\text{ cm}) > 0$. (The weaker restriction at 6 cm is to avoid biasing the results against strongly nonthermal emission.) Even though the data involve a scaled-array pair, the numerical values of the spectral index α may be questioned since the VLA is not a filled aperture. As one test we checked the values of the spectral index α (defined so that $S_\nu \propto \nu^\alpha$) for radio sources that coincide with Hα sources. We find that in nearly all cases with sufficiently high signal-to-noise ratio, these sources show a patch which is consistent with optically thin free-free emission, i.e., a region of at least 25 pixels in which every pixel has $\alpha = -0.1 \pm 0.2$. In particular, a large H II region complex along the southern part of the eastern arm has such a patch with an equivalent diameter of 30″. Thus even for a somewhat extended source, the discrepancy between the true spectral index and the value deduced from this map is not large.

PLATE 8

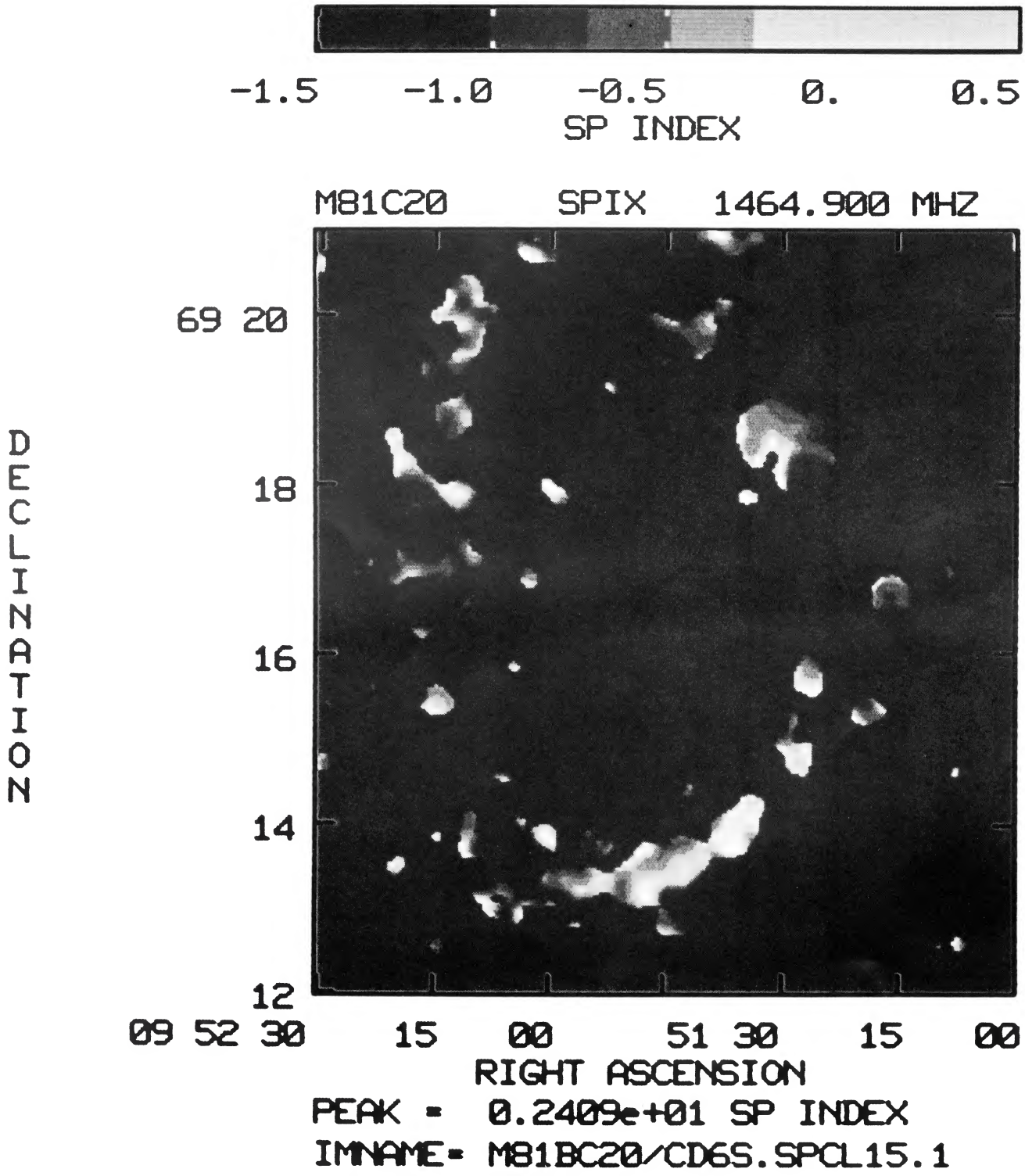

FIG. 7*a*

FIG. 7.—(*a*) Spectral index map of part of the M81-S field. This map, constructed from maps 7 and 8 in Table 3, shows the eastern arm with a resolution of 15″ × 15″. The gray-scale display is adjusted to reveal the H II regions. The bright source in the nucleus was removed from the data. (*b*) Spectral index map of the M81-S field with a resolution of 18″.2 × 18″.2. This map was constructed from maps 6 and 13 in Table 3. The gray-scale display is adjusted so that strongly nonthermal emission would be easier to see than in Fig. 7*a*. The bright source in the nucleus was removed from the data.

BASH AND KAUFMAN (*see* page 627)

For the more extended arm emission, the uncertainty in the value of α is greater because of poorer signal-to-noise ratio. With this in mind, we characterize the extended emission along the arms as mildly nonthermal; most of the extended emission has α more negative than in the H II regions, but less negative than in source number 57 where we obtain $\alpha = -1.0 \pm 0.1$. As a second test of spectral index values for the M81-S field, we constructed another spectral index map (shown in Fig. 7*b* [Pl. 9]); for this map we replaced map 7 of Table 3 by map 6, interpolated map 6 to the same coordinate grid as map 7 and then convolved the 6 and 20 cm data to an 18".2 × 18".2 beam. Map 6 differs in tapering, cleaning, and beam width from the 6 cm map used to produce Figure 7*a*. With the lower resolution, the values of α for the H II regions came out somewhat more negative (typically $\alpha = -0.2$ to -0.4), as might be expected if the beam includes both the H II region and surrounding nonthermal arm emission. The values of α for extended arm emission remained roughly the same as in the spectral index map of Figure 7*a*.

The values of α for the extended emission appear typical of values seen in supernova remnants. This may simply be the result of mixing diffuse thermal and nonthermal radiation. Or, if the radiation is primarily synchrotron emission from relativistic electrons that have leaked into the interstellar magnetic field from SNRs, then the electron energy spectrum has not steepened appreciably.

For the M81-N field the only 6 cm data available are from the C array. As a test of these data, we have made the following two maps, both interpolated to the same coordinate grid and convolved to the same 10" × 10" beam as the 20 cm map in Figure 2: (1) a 6 cm map (map 9 in Table 3) from C array data for M81-N, and (2) a 6 cm map (map 10) from the C and D array data for M81-S. In Figure 8 we compare the 6 cm fluxes for the eight sources common to these two maps, that is, the sources with primary beam attenuation factor f_{PB} less than 4 on both maps. The flux values on these two maps are designated S_ν(6N) and S_ν(6S), respectively, and the corresponding spectra index values (for the 20–6 cm range) are denoted α(N) and α(S). Three of the eight sources coincide with Hα sources; for these three giant H II regions, the values of S_ν(6N) and S_ν(6S) are in good agreement although the uncertainties are large. The error bars in Figure 8 indicate $\sigma A^{1/2} f_{PB}$, where A is the source area divided by the synthesized beam area. The average value of $S_\nu(6N)/S_\nu(6S)$ for the eight sources is 1.2. Figure 9 shows how the values of α(N) and α(S) compare for these sources. For both determinations of the spectral index we used the 20 cm map (map 2 in Table 3) derived from B and C array data; thus α(S) is based on a scaled-array pair but α(N) is not. Nevertheless, for the three giant H II regions the values of α(N) and α(S) agree and are consistent with optically thin free-free emission. A least-squares fit to the eight sources gives

$$\alpha(N) = (1.09 \pm 0.38)\alpha(S) + 0.15 . \quad (1)$$

A spectral index map for the M81-N field would not indicate anything meaningful about the extended emission along the arms since we do not have 6 cm D array data for this region. However, it is useful for showing that most of the bright knots in the western arm are optically thin free-free sources (see Fig. 10 [Pl. 10]). In Kaufman *et al.* (1986*b*) we compare the radio and Hα fluxes of the giant H II regions and of possible SNR'S.

c) Polarization

We have looked for linear polarization on the various maps listed in Table 3. In § V we shall consider several polarized background sources. In the nucleus of M81 we detect significant polarized intensity above the 3 σ level on both the 6 and 20 cm maps at the following positions: (1) in source number 68 and (2) in the extended emission around the compact nuclear source. We shall describe this in a separate paper on the nucleus of M81. Along the spiral arms we find only a few small patches with peak polarized intensity above the 3 σ level. These unresolved polarized features are described in Table 4. For each polarized region we list the map (see Table 3) on which the polarization is detected, the plane-of-sky distances X-X_N, Y-Y_N from the compact source in the nucleus, with X positive to the east and Y positive to the north, the flux density S_ν

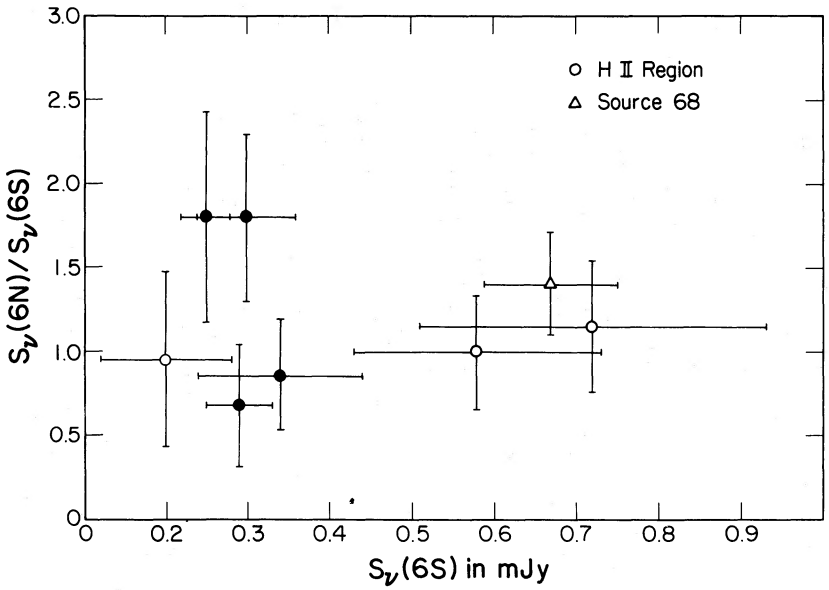

FIG. 8.—A comparison of 6 cm flux densities for eight sources that occur in both the M81-N and M81-S fields. The values of S_ν(6N) are derived from map 9, while the values of S_ν(6S) are derived from map 10.

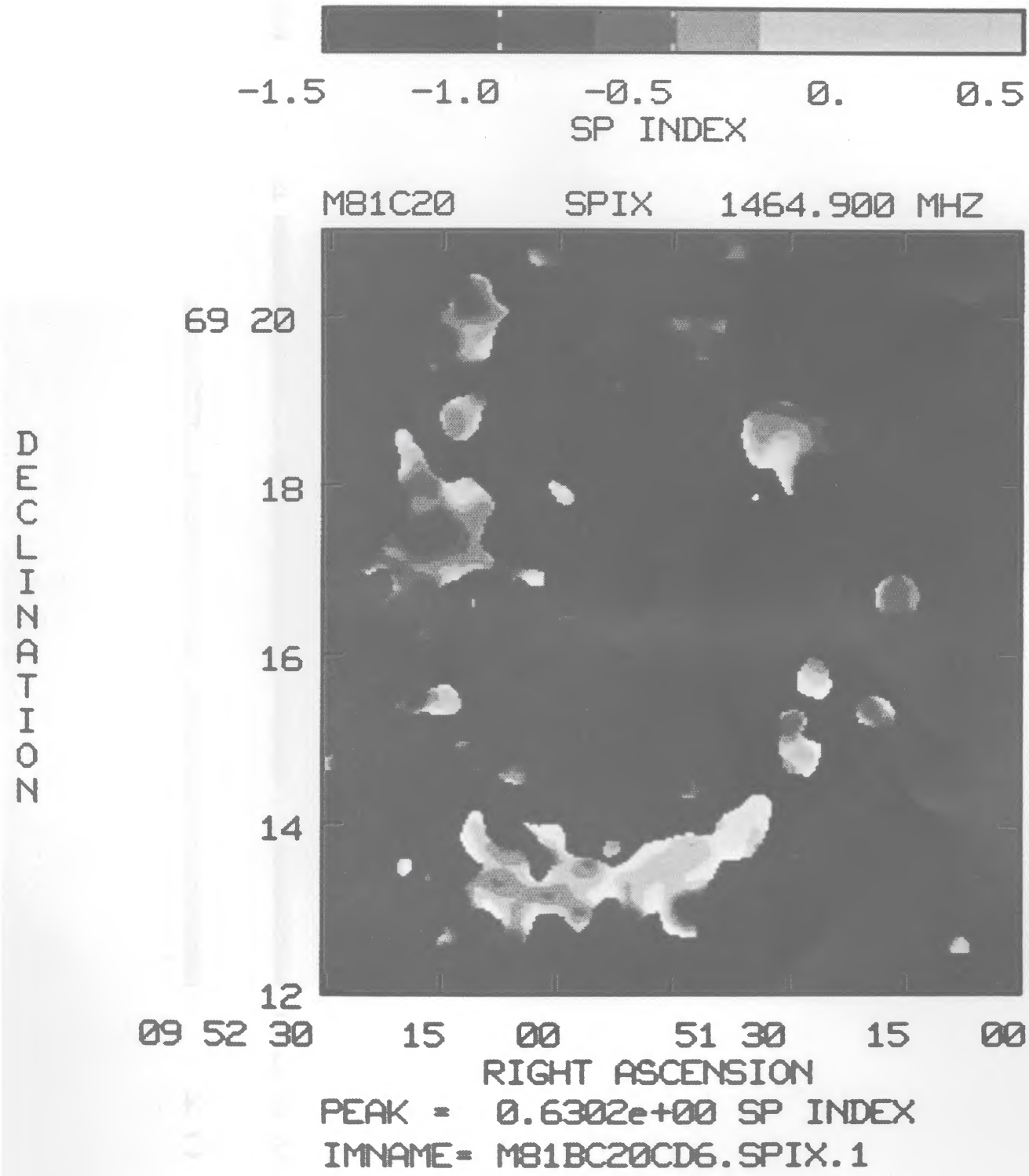

FIG. 7*b*

BASH AND KAUFMAN (*see* page 628)

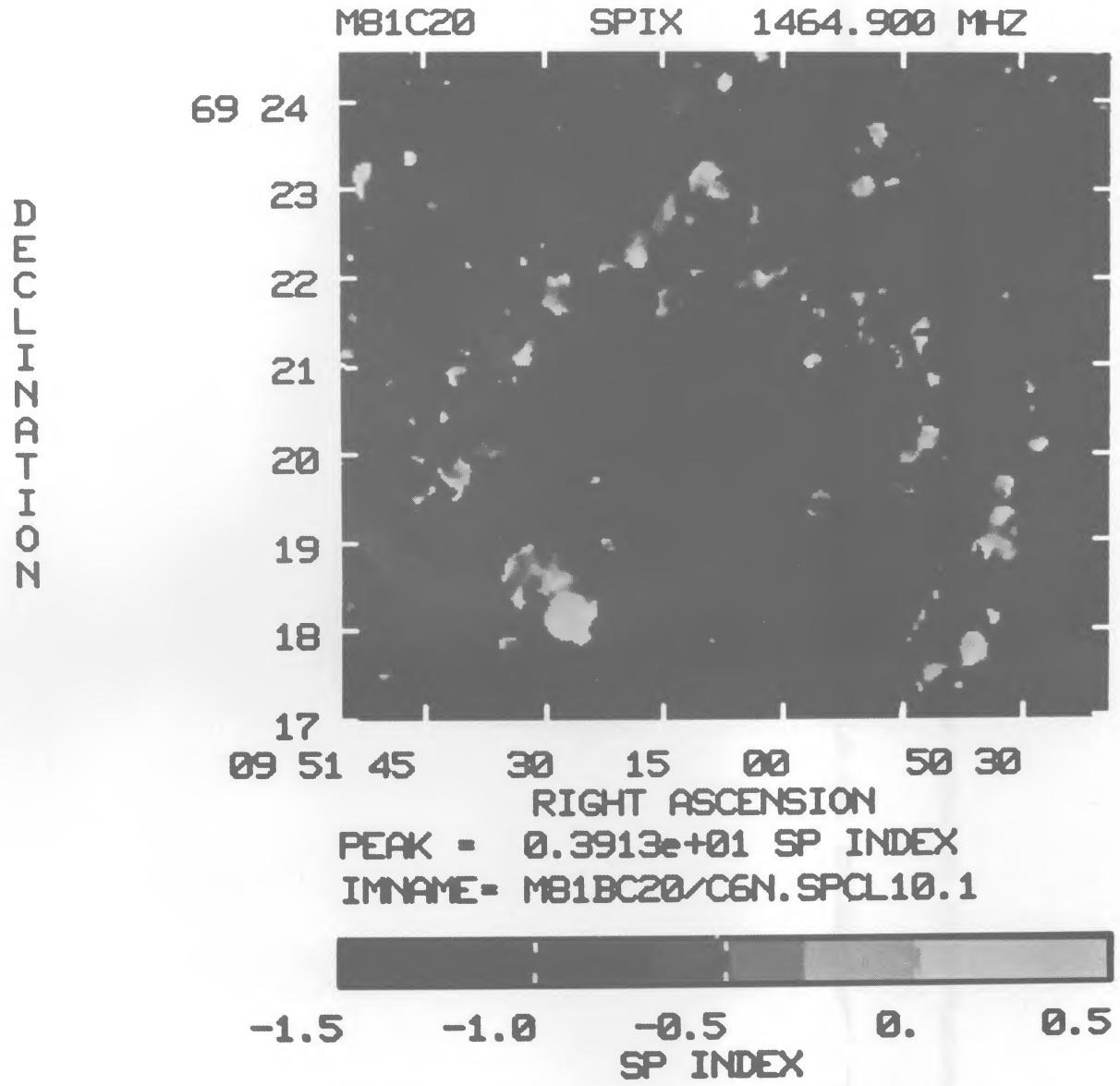

FIG. 10.—Spectral index map of part of the M81-N field. This map, constructed from maps 2 and 9, shows the nucleus and the western arm with a resolution of 10″ × 10″.

BASH AND KAUFMAN (*see* page 628)

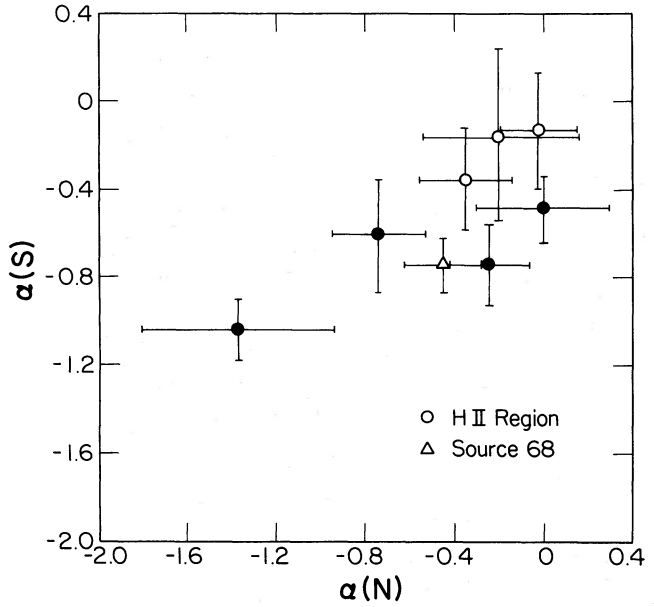

FIG. 9.—Comparison of the values for the spectral index $\alpha(N)$ derived from maps 2 and 9 with the values for the spectral index $\alpha(S)$ derived from maps 2 and 10 for the eight sources in common.

measured on the corresponding total intensity map, and the percentage polarization averaged over the polarized feature. Notice that the values for the percentage polarization have large uncertainties; therefore, these regions are best characterized as possibly polarized features. Also, a small weak source in the interarm region near the eastern minor axis appears to be polarized on our lowest resolution 20 cm map. Since this polarized feature lies in the interarm region, it may be an artifact on the polarized intensity map or a background source.

Beck, Klein, and Krause (1985) and Segalovitz, Shane, and de Bruyn (1976) detect regions of polarized emission in M81 near the minor axis, but the 2′–2.′45 resolution of the maps in these papers is too poor to separate arm from interarm emission here. For example, in Beck *et al.* a large polarized source west of the nucleus seems to lie mainly in the interarm region while the one east of the nucleus overlaps both spiral arms. They note that if the magnetic field vectors are parallel to the spiral arms, then the percentage polarization should be maximum near the minor axis, as suggested by their data. R. Beck, M. Krause, and E. Hummel (1985, private communication) have taken VLA observations of M81 at 20 cm with D array and combining their data with ours to study the polarization further with better resolution than their MPIfR data affords.

Perhaps our failure to find much evidence for polarization along the arms is not too surprising when one considers the signal-to-noise ratio for the nonthermal arm emission on our maps. On our total intensity map at 20 cm that is most sensitive to extended emission (map 12 in Table 3), a typical value for the intensity of the nonthermal arm emission peaks is 4–6 σ (see § IV). If we allow for the factor of 2.8 lower noise on the corresponding polarized intensity map (map P2), then a typical nonthermal arm feature will be below 3 σ on the polarized intensity map if its polarization is less than 18%–27%. With much lower resolution Segalovitz, Shane, and de Bruyn (1976) report a few 21 cm polarization peaks at the 20% level, close to our upper limits. Our most sensitive total intensity map at 6 cm (map 6), shows the field M81-S, where the eastern arm is prominent. On this map the values of the peak nonthermal arm emission are usually 4–5.5 σ near the major axis and tend to be smaller near the minor axis, in part, because of primary beam attenuation. Allowing for the lower noise on the corresponding polarized intensity map (map P5), we note that unless these features have polarization greater than 28%–38%, they will be lost in the noise. Since we failed to detect these sources along the arms in the polarized intensity map, we conclude that the sources along the eastern arm have polarizations $\lesssim$40% at 6 cm. Because of possible Faraday depolarization at 20 cm and the question of the orientation of the magnetic field with respect to the line of sight, our upper limits on the percentage polarization of the arms do not impose much of a constraint on the degree of ordering of the magnetic field.

IV. ARM WIDTHS

To study the intensity profiles across the arms, we have taken slices perpendicular to the arms at 26 different locations selected so that the slices do not go through the giant radio H II regions. Therefore, the intensity profiles characterize the extended emission from the spiral arms.

Figure 11 (Plate 11) shows the locations of a representative set of these slices, and Figures 12 and 13 show the corresponding intensity profiles. For each arm the intensity profiles are displayed in plane-of-the sky coordinates and are listed in order of distance from the nucleus. We indicate on each profile (1) the beam width θ in the plane of the sky and (2) a scale length equivalent to 1 kpc in the plane of M81. All features with intensity $I_v > 2\ \sigma$ are labeled. To project a 1 kpc length from the plane of M81 to the plane of the sky, we adopt an inclination of 59° and a position angle of 149° for the major axis, as in Visser (1980).

The 20 cm map used to produce the set of profiles in Figure 12 has a 9.″2 × 9.″7 beam and is our best 20 cm map for detecting a spiral shock ridge with width $\leq$190 pc. The intensity profiles across the arm reveal that the extended emission is spotty and often rather weak, but generally the width of the emission is several times the beam width. While one might possibly explain a broad arm in the northern part of M81 as resulting from tidal perturbations by M82, the 20 cm arms are

TABLE 4

POLARIZED FEATURES ALONG THE ARMS

X-X_N	Y-Y_N	λ (cm)	Map in Table 3	S_v (mJy)	Percentage of Polarization	Comments
149″.....	18″	6	5P	0.24 ± 0.05	24 ± 12	On inner ring
140	−288	6	5P	0.21 ± 0.05	26 ± 13	On southern part of east arm
−118	277	20	1P	0.35 ± 0.07	32 ± 12	On northern part of west arm

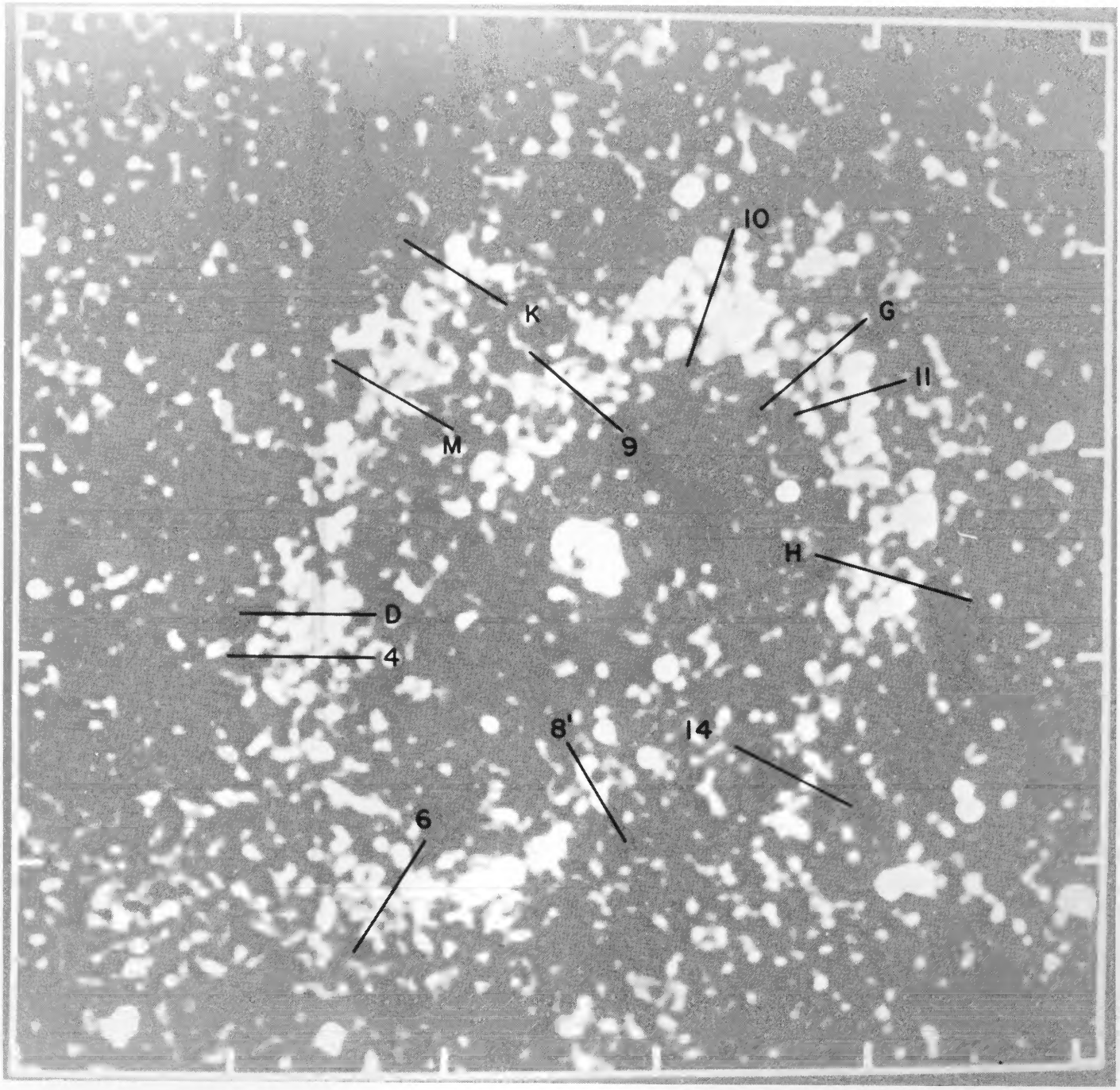

FIG. 11.—The locations of the slice profiles displayed in Figs. 12 and 13

BASH AND KAUFMAN (*see* page 629)

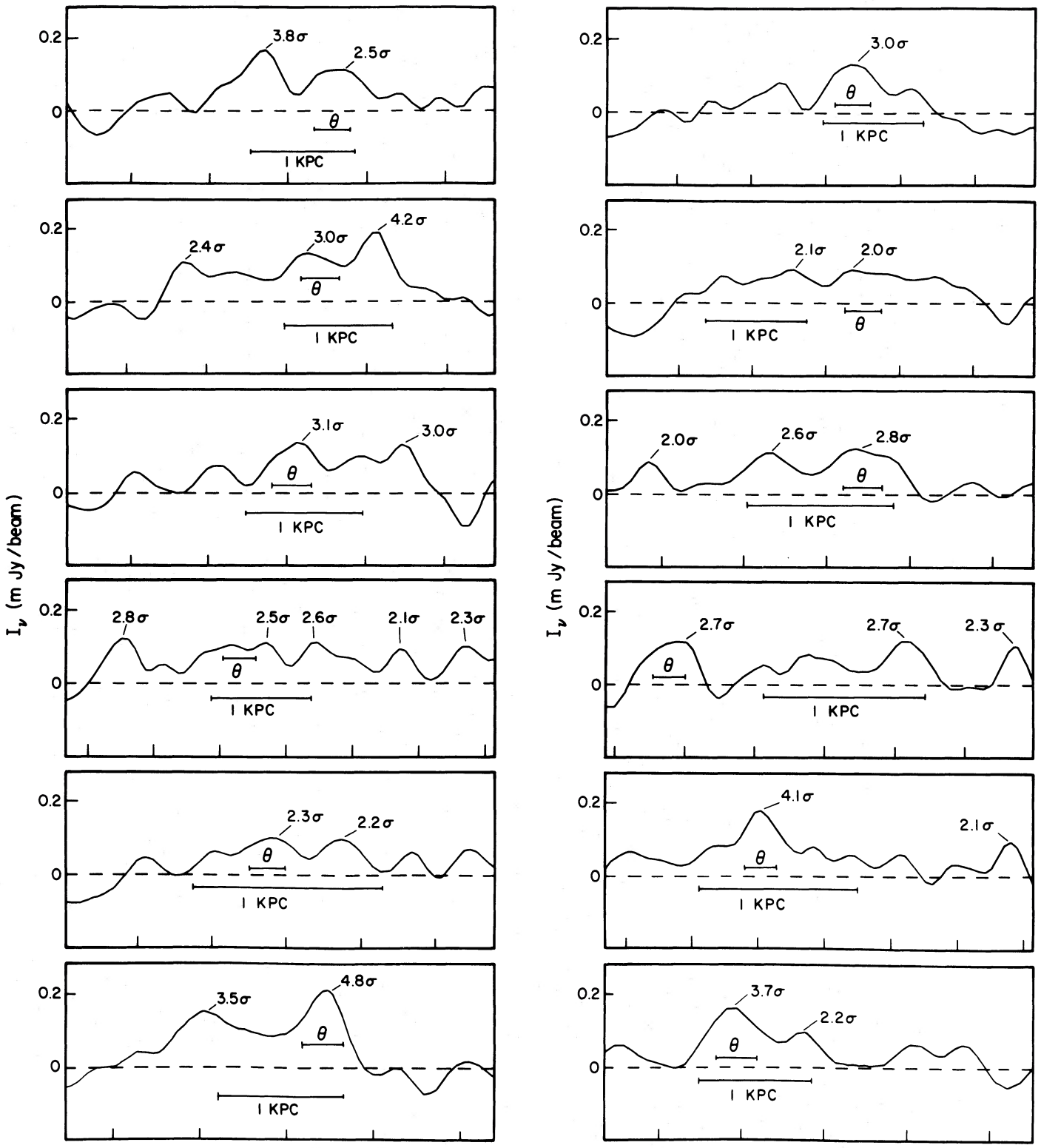

FIG. 12*a*

FIG. 12*b*

FIG. 12.—Examples of 20 cm intensity profiles across the arms on map 11, which has a resolution of 9″.2 × 9″.7. The profiles are displayed from top to bottom in order of decreasing distance from the nucleus. Fig. 12*a* shows the east arm; Fig. 12*b*, the west arm. The indicated scale length is equivalent to 1 kpc in the plane of M81; θ is the beam width in the plane of the sky. The profiles are in plane-of-the-sky coordinates and have not been corrected for primary beam attenuation.

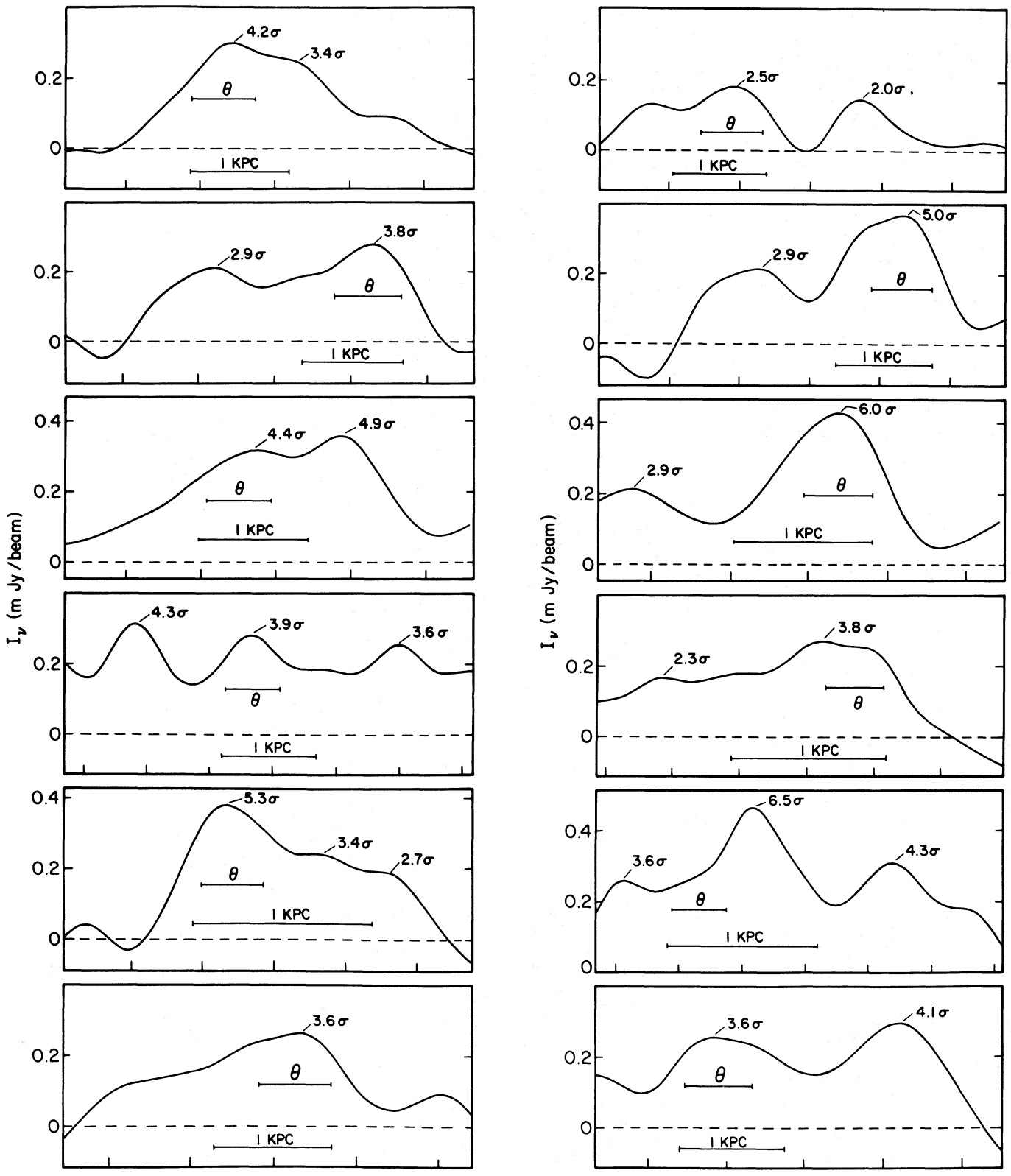

FIG. 13*a*

FIG. 13*b*

FIG. 13.—Same as Fig. 12 but for map 12, which has a resolution of 17″.4 × 17″.2

also well resolved in the rest of the galaxy. Either the scale height of the shocked layer is at least 4 times the value Visser adopts for the H I disk and one is seeing significant layer smearing, or the radio continuum arms are much broader than predicted by a hydrodynamic calculation for a single component medium.

Since the arms are clearly resolved with the 9".2 × 9".7 beam, we expect to gain in sensitivity by using a broader synthesized beam. Figure 13 shows the intensity profiles for the same slice locations, but on a 20 cm map with a 17".4 × 17".2 beam. Although the rms noise per beam area is higher on this map (see Table 3), the profiles in Figure 13 have a higher signal-to-noise ratio than those in Figure 12. This confirms that the arms are broader than the beam of Figure 12. Even with the broader beam of Figure 13, the arms are still clumpy and well resolved. In most cases the arm width is 1–2 kpc. For the M81-S field we have looked at intensity profiles on the 6 cm map of Figure 6 where the beam is 18".2 × 17".8. While the nonthermal extended emission has greater intensity on the 20 cm map used in Figure 13, the 6 cm map has lower noise. For positions where the primary beam attenuation is small, the 6 cm map is twice as sensitive to emission that fills the beam. The values derived for the arm widths on this 6 cm map are similar to those deduced from the 20 cm map.

The observed 1–2 kpc width of the radio continuum arms is too broad for a hydrodynamic density wave model unless the shocked layer has a large scale height. If Visser's (1980) values for the scale height of the H I disk apply to the shocked layer, then the predicted width of the radio continuum ridge in the plane of the sky would be at most 260 pc (after deconvolution from the synthesized beam). The observed arm width agrees better with the 1 kpc width predicted for the density enhancement in the cloudy density-wave model of Roberts and Hausman (1984) and Hausman and Roberts (1984) for our Galaxy. Hine and Rots (1986) have used the VLA to map M81 in H I with a resolution of 9". On comparing the observed velocity profiles with the predictions from Visser's model, they conclude that the width of the shocked layer is greater than predicted by the hydrodynamic calculations and agrees better with the cloudy models of Roberts and Hausman. Thus both the H I data and the radio continuum data point to the same conclusion.

V. BACKGROUND SOURCES

From the VLA surveys listed in Condon and Mitchell (1984), we estimate the expected number of background sources at 20 cm for the area shown in Figure 14. The numbered sources in Figure 14 are selected as probable background sources and have values of $S_\nu(20\text{ cm}) > 0.35$ mJy. For this 436 arcmin^2 region we list the expected number of background sources in the second column of Table 5 and the observed number in the third column. All of these sources lie within the 30'.4 primary half-power beam. We restrict source counts to the region in Figure 14 because cleaning the map did not completely remove the sidelobes of the strong sources 1 and 124 (labeled in Fig. 1). All of the numbered sources in Figure 14 with $S_\nu(20\text{ cm}) > 1$ mJy are also present in the WRST map of Segalovitz (1977). Defining physical doubles according to the convention of Condon and Mitchell (1984), we list as a single source the sum of all components that have angular separation less than 1' and comparable flux densities.

For $S_\nu(20\text{ cm}) > 0.6$ mJy, the predicted and observed background source counts agree. This suggests that almost all the brighter sources along the spiral arms are associated with M81; in particular, the two sources (number 57 and 75) that line up with the nucleus near the inner endpoints of the spiral arms are probably part of M81. On the other hand, for $S_\nu(20\text{ cm}) = 0.35$–$0.60$ mJy the predicted number of background sources in Figure 14 is 10.3 ± 2.2. At this level it is less clear as to which peaks should be classified as background sources, particularly in the faint outer extensions of the arms. Taking a conservative view, we label two sources, number 114 and 111, as background sources, but our list is clearly incomplete. For $S_\nu(20\text{ cm}) < 0.6$ mJy, we expect some chance coincidences between background sources and those associated with M81.

TABLE 5

BACKGROUND SOURCE STATISTICS

$S_\nu(20\text{ cm})$ (mJy)	Expected Number	Observed Number
>0.60	15.1 ± 2.2	12
>1	10.3 ± 1.7	9
>2	6.2 ± 1.3	6
>5	3.2 ± 0.6	3

We have checked the larger region shown in Figure 1 for coincidences between 20 cm sources and optical objects listed in Dixon and Sonneborn (1980). None of the 15 Zwicky-Luyten ultrafaint blue stars in this field appear in our data. However, two of the 20 cm sources coincide with faint galaxies: the Magellanic irregular BEM 2 (Bertola and Maffei 1974) with our radio source number 2 and the galaxy Keel 191 (Keeler 1900) with radio source number 114. There is a chance coincidence between the outer part of the galaxy MAI 048 (Mailyan 1973) and the bright polarized radio source number 124. Four other galaxies listed for this field by Dixon and Sonneborn do not show up in our data.

Table 6 lists our data on various probable background sources. The values of the flux density $S_\nu(20\text{ cm})$ result from summing the pixel intensities within a rectangular box around the source on the maps shown in Figures 1 and 2. The uncertainties listed are

$$\sigma_T = [(\sigma f_{\rm PB})^2 A + (0.01 S_\nu)^2]^{1/2}\,, \qquad (2)$$

where the 1% calibration error term is significant compared to the rms noise only for the strongest sources. We also did two-dimensional Gaussian fits to each source; except for sources 88 and 58, the flux values obtained from the Gaussian fits differ by less than 7.5% from the values obtained by summing the pixel intensities. To estimate the source diameters, we start with the source half-power diameters given by the two-dimensional Gaussian solution, correct these for bandwidth smearing by using the graph in Bridle (1982), and then deconvolve from the synthesized beam. The result is that only three of the sources in Table 6 show some indication of being resolved with the 12".4 × 12".7 beam of the map in Figure 1.

A number of the background sources also appear on our 6 cm maps, but only six of these have primary beam attenuation factor $f_{\rm PB} < 5$ at 6 cm. Three of the six sources are clearly nonthermal. Among the sources in Table 6, we detect a significant polarized intensity in only the three brightest sources. The percentage polarization values listed are averaged over the source.

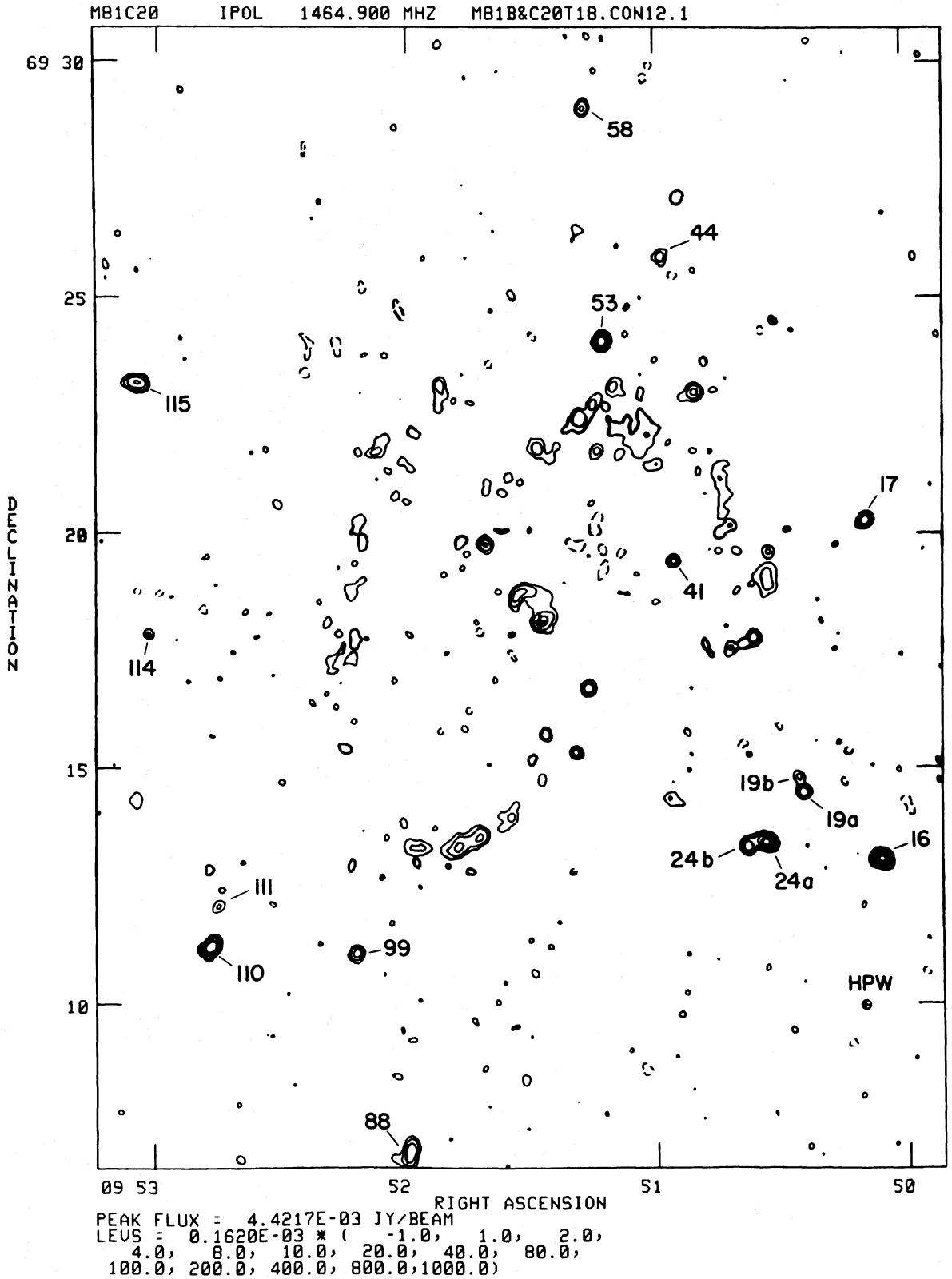

FIG. 14.—The locations of 20 cm background sources on map 3. The numbered sources are used for computing background source statistics.

TABLE 6

BACKGROUND SOURCES

Source	X-X_n[a]	Y-Y_n[a]	S_ν(20 cm) (mJy)	α[b]	Percent of Polarization	Size
16	−435″	−303″	7.04 ± 0.21	*	3 ± 1	...
110	423	−413	5.63 ± 0.24	*	...	...
24a	−286	−281	3.57 ± 0.15	*	...	4″ × 3″
24b	−263	−287	1.63 ± 0.13	−0.4 ± 0.2:	...	...
88	170	−677	4.89 ± 0.35	...	...	...
115	515	304	3.58 ± 0.25	...	...	...
53	−77	356	3.52 ± 0.15	−0.7 ± 0.1	...	...
19a	−334	−218	1.37 ± 0.13	*	...	...
19b	−328	−198	0.44 ± 0.11	*	...	...
17	−413	129	1.47 ± 0.16	−1.1 ± 0.4	...	...
99	237	−422	1.40 ± 0.16	−0.4 ± 0.2	...	...
58	−53	653	0.90 ± 0.17	...	...	...
44	−152	464	0.86 ± 0.14	−0.0 ± 0.4	...	...
41	−169	77	0.78 ± 0.11	−0.7 ± 0.2	...	...
111	413	−361	0.49 ± 0.11	...	...	...
114	502	−15	0.38 ± 0.11	...	...	...
2[c]	−763	−232	2.66 ± 0.40	...	...	...
1[c]	−764	−1	85.8 ± 0.9	...	4.5 ± 0.2	11 × 3
124[c]	712	404	56.8 ± 0.7	...	2.6 ± 0.3	6 × 6

[a] Distance from the nucleus of M81 with X positive to the east, Y positive to the north.

[b] The value of α is listed if f_{PB}(6 cm) < 3.5 and the uncertainty in S_ν(6 cm) < 45% (or, with a colon if f_{PB}(6 cm) = 3.5–5). An asterisk indicates that the source was detected at 6 cm but does not meet these conditions.

[c] Outside of the region chosen for source statistics.

VI. THE PITCH ANGLES OF THE SPIRAL ARMS

The symmetry of the two spiral arms is shown in Figure 15 (Plate 12), which displays a 20 cm map deprojected into the plane of M81. This map was made from B and C array data with the bright nucleus removed. After transforming this map into R, ϕ coordinates, where R is the galactocentric radius and ϕ is the azimuthal angle, we traced the arms by eye and obtained the values shown in Figure 16 for ln R versus ϕ. Because the patchy character of the emission made it difficult to work with the inner edge of the 20 cm arms, the positions plotted in Figure 16 represent roughly the locus of arm centroids. Our choice of spiral curve for each arm is strongly influenced by the giant radio H II regions, and thus these spirals also represent the location of the most active star formation along the arms.

In density wave theory, the spiral arms are approximately logarithmic spirals, but since the pitch angle of the potential minimum depends on the rotation curve and the stellar velocity dispersion, some variation of pitch angle with R is possible. In his model for M81, Visser (1980) chooses a stellar velocity dispersion that decreases as R increases so that the pitch angle of the potential minimum varies from 11° at 3.′2 to 16° beyond 6.′9, close to the values observed for the H I and optical arms (see Table 7). Visser points out that as a result of the orbital motions of the clouds, the pitch angle of the spiral arms defined by the young stars is not necessarily the same as the pitch angle of the potential minimum. Furthermore, in the cloudy density wave model of Hausman and Roberts (1984), the distribution of stellar associations may show local deviations from a symmetric pattern as a result of (1) chance fluctuations in the distribution of clouds, (2) sequential star formation, and (3) the local effect of the kinetic energy input from supernova explosions. Indeed, from his optical study of 113 galaxies, Kennicutt (1981) concludes that both small-scale and large-scale distortions are a general feature of spiral arm geometry.

If each radio continuum arm in M81 were a logarithmic spiral of constant pitch p, then the curves in Figure 16 would be straight lines with slope tan p. It is clear that a logarithmic spiral is only an approximate fit. As R decreases from 9.′5, the pitch angle is nearly constant as the azimuth changes by 80° (east arm) or 120° (west arm), but then both curves in Figure 16 go through a depression. For the western arm the bump is more pronounced and occurs in the northern part of M81 where tidal perturbations by M82 may have played a role. For

TABLE 7

VARIOUS DETERMINATIONS OF THE PITCH ANGLES OF THE SPIRAL ARMS IN M81

	Region Fitted				
Spiral Tracer	R	ϕ	Arm	p	Reference
20 cm emission	4.′3–10.′3	0°–195°	East	13°.6 ± 0°.4	This paper
	6.6–10.3	110 –195	East	17.4 ± 0.8	This paper
	4.6–9.5	70 –180	West	22.6 ± 0.4	This paper
H I	3.2–10.6	...	Both	15	Rots 1975
Optical	near 4.3	...	Both	11	Oort 1974
	near 9.5	...	Both	17	Oort 1974
Blue light and Hα	...	...	Both	12 ± 2	Kennicutt 1981

PLATE 12

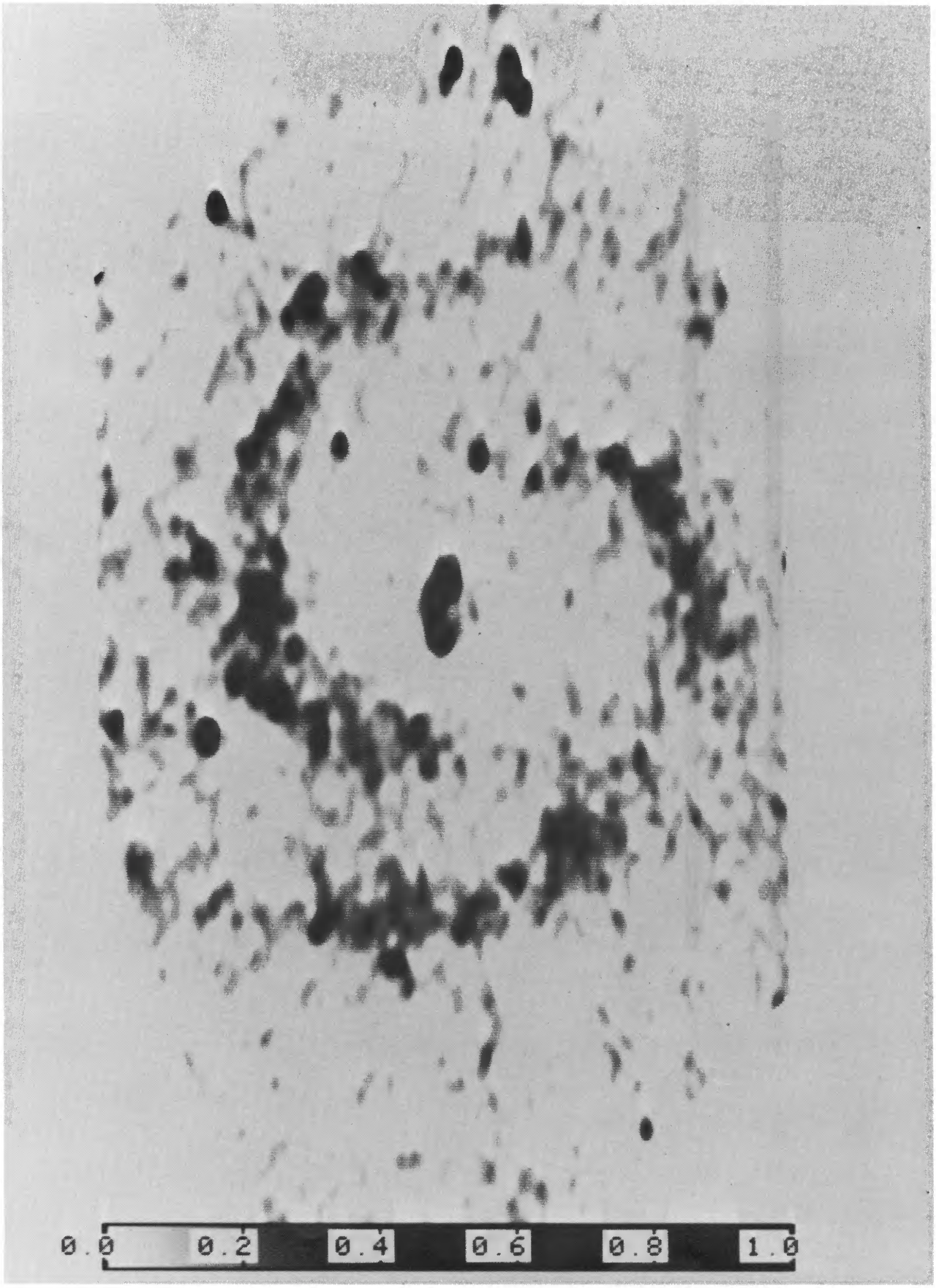

FIG. 15.—The 20 cm emission deprojected into the plane of M81. This is a deprojected version of map 8. The bright source in the nucleus was removed from the data.

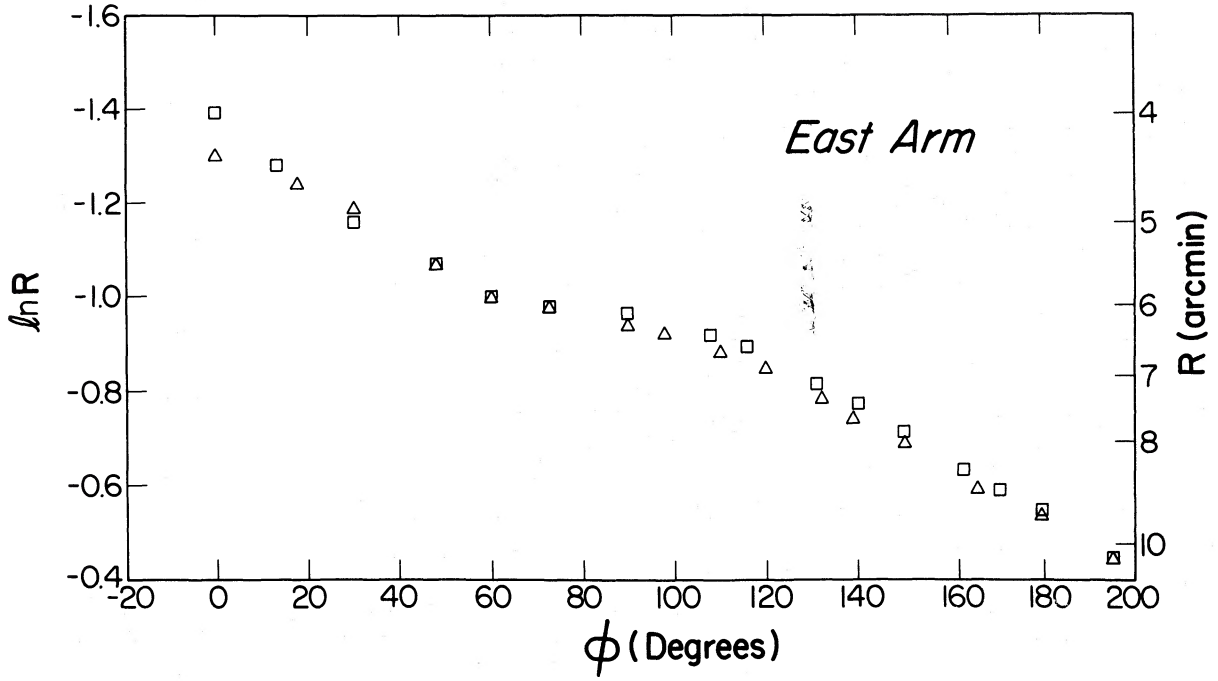

FIG. 16*a*

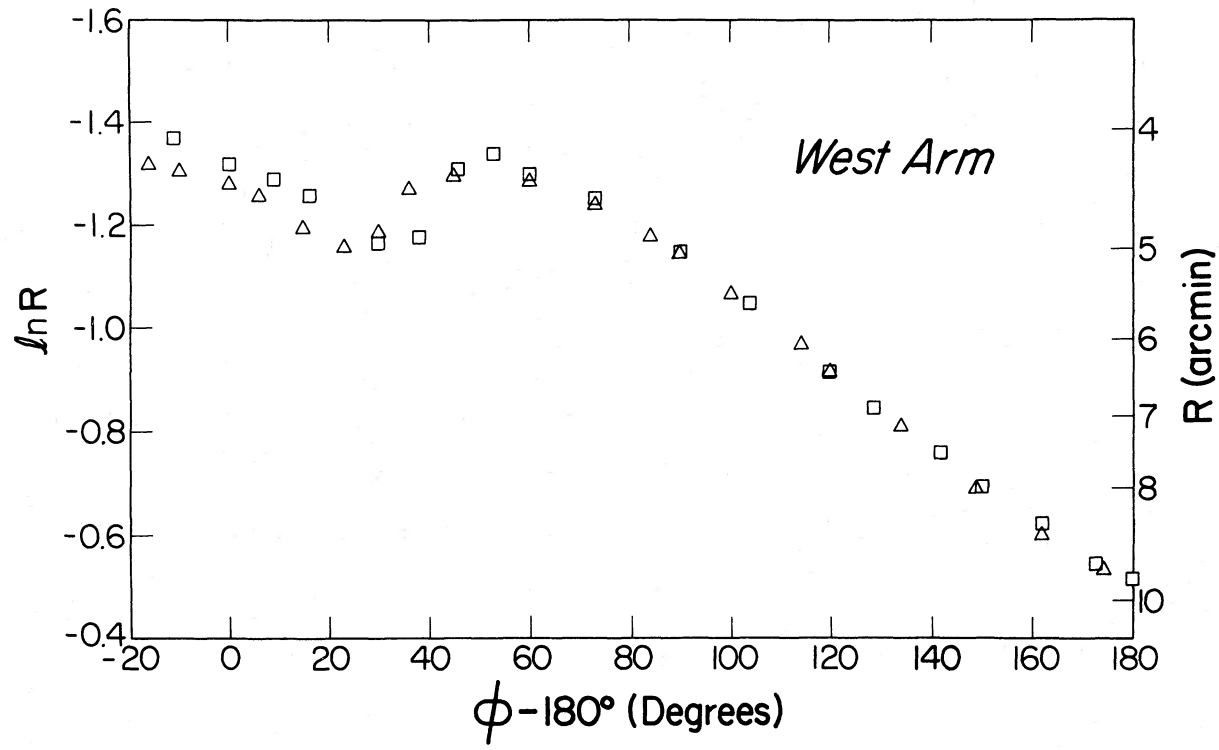

FIG. 16*b*

FIG. 16.—Measured values of ln R vs. ϕ for the 20 cm arms. The zero point for ϕ was chosen arbitrarily, but it is the same in both graphs. Each plot shows the result of two estimates of the spiral arm location.

both arms the distortions occur over the range of R where M81 has the greatest concentration of giant radio H II regions. Here one expects a higher frequency of supernovae, and perhaps the distortions are associated, in part, with the increased kinetic energy input from past supernova explosions.

Table 7 lists the values we obtain for the pitch angles; our values are the average of two estimates of the spiral position for each arm. For the east arm the pitch angles for the 20 cm arm are similar to values previously derived from H I and optical data. In Paper II we shall compare the location of these spirals with the spiral curve defined by the velocity shock in the H I gas.

VII. CONCLUSIONS

The following are the main results of our VLA observations of M81 at 6 and 20 cm.

1. We detect both thermal and nonthermal radiation from the spiral arms. On maps with a resolution of 10″–15″, we separate giant H II regions from the more extended, nonthermal arm emission and find that most of the bright knots along the radio arms are giant radio H II regions.

2. The nonthermal emission defines spiral arms that are patchy and well-resolved, with a width of 1–2 kpc. The observed nonthermal arms are too broad to agree with the continuum gasdynamical calculations of Roberts (1969), Shu *et al.* (1972), and Visser (1978, 1980) for a classical density wave model. This is a surprising result. To get the observed width of the nonthermal arms to agree with Visser's hydrodynamic model for M81 would require a scale height for the shocked layer 4–8 times the scale height adopted by Visser for the H I disk. Furthermore, since Visser's theoretical value for the shock width is smaller than that deduced from the H I velocity map of M81 made by Hine and Rots (1986), the discrepancy is not peculiar to just the synchrotron radiation.

3. On the other hand, the observed arm widths appear consistent with the predictions of density-wave models that emphasize the clumpy nature of the interstellar medium. For example, in the cloudy density wave model of Roberts and Hausman (1984) for our Galaxy, the density enhancement is 1 kpc wide. It would be interesting to see what their model would predict if the input parameters were appropriate to M81.

4. The 20 cm arms appear to spiral outward from a faint inner H I ring. This suggests that the H I ring is produced by the inner Lindblad resonance and thus places the ILR near a galactocentric radius R of 4′ rather than at the 2′.6 value adopted by Visser (1980).

5. Our upper limits on the degree of polarization of typical nonthermal emission peaks along the arms are 18%–27% at 20 cm and 28%–38% near the southern major axis at 6 cm.

6. At large R the radio continuum arms are approximately logarithmic spirals although the two arms differ in pitch angle. Distortions in the spiral arm geometry seem to occur where the concentration of giant radio H II regions is greatest and in the north, where tidal effects by M82 may have been important.

7. The alignment of radio sources in the central region of M81 tends to give a barlike or jet like appearance to the nucleus. Two of these sources lie on a line through the compact source and are situated near the inner endpoints of the 20 cm arms.

We thank the NRAO staff at the VLA site and in Charlottesville for their invaluable assistance. In particular, we thank Dick Sramek, Peggy Perley, Rick Perley, and Barry Clark for helping us at the VLA and Bill Cotton, Eric Greisen, Gary Fickling, Kerry Hildrup, Don Wells, Fred Schwab, Barry Turner, Bob Lang, and Ed Fomalont for helping us use the AIPS reduction programs and for answering our many questions. We also thank David Leisawitz for help in making the observations and Kristin Barker at The University of Texas for assisting with some of the data reduction. This work was supported in part by grants to M. K. from the American Astronomical Society Small Research Grant Program and to F. B. from the National Science Foundation, grant AST83-12332. M. K. thanks the Department of Mechanical Engineering at The Ohio State University for use of their VAX computer.

REFERENCES

Bash, F. N., and Peters, W. L. 1976, *Ap. J.*, **205**, 786.
Bash, F. N., and Visser, H. C. D. 1981, *Ap. J.*, **247**, 488.
Beck, R. 1983, private communication.
Beck, R., Klein, U., and Krause, M. 1985, *Astr. Ap.*, **152**, 237.
Bertola, F., and Maffei, P. 1974, *Astr. Ap.*, **32**, 117.
Bottinelli, L., Gouguenheim, L., Paturel, G., and de Vaucouleurs, G. 1984, *Astr. Ap. Suppl.*, **56**, 381.
Bridle, A. H. 1982, *Synthesis Mapping, Proceedings of the NRAO-VLA Workshop*, ed. A. R. Thompson and L. R. D'Addario (Greenbank, W. Va: NRAO), p. 14-1.
Condon, J. J., and Mitchell, K. J. 1984, *A.J.*, **89**, 610.
de Vaucouleurs, G. 1981, private communication.
Dixon, R. S., and Sonneborn, G. 1980, *A Master List of Nonstellar Optical Astronomical Objects* (Columbus, O.: Ohio State University Press).
Elmegreen, D. M. 1981, *Ap. J. Suppl.*, **47**, 229.
Elmegreen, D. M., and Elmegreen, B. G. 1983, *Ap. J. Suppl.*, **54**, 127.
Emerson, D. T., Kronberg, P. P., and Wielebinski, R. 1978, *Astr. Ap.*, **63**, 49.
Hausman, M. A., and Roberts, W. W. 1984, *Ap. J.*, **282**, 106.
Hine, B. 1984, M.A. thesis, University of Texas.
Hine, B., and Rots, A. H. 1986, in preparation.
Kaufman, M., Bash, F. N., Hine, B., Rots, A. H., Kennicutt, R. C., Hodge, P. W., and Elmegreen, B. G. 1986*a*, in preparation (Paper II).
Kaufman, M., Bash, F. N., Kennicutt, R. C., and Hodge, P. W. 1986*b*, in preparation.
Keeler, J. E. 1900, *Ap. J.*, **11**, 325.
Kennicutt, R. C. 1981, *A.J.*, **86**, 1847.
Leisawitz, D., and Bash, F. N. 1982, *Ap. J.*, **259**, 133.
Lin, C. C., and Shu, F. H. 1964, *Ap. J.*, **140**, 646.
Mailyan, N. Sh. 1973, *Astrofizika*, **9**, 63.
Mathewson, D. S., Kruit, P. C., and van der Brouw, W. N. 1972, *Astr. Ap.*, **17**, 468.
Oort, J. H. 1974, in *IAU Symposium 58, The Formation and Dynamics of Galaxies*, ed. J. R. Shakeshaft (Dordrecht: Reidel), p. 375.
Roberts, W. W. 1969, *Ap. J.*, **158**, 123.
Roberts, W. W., and Hausman, M. A. 1984, *Ap. J.*, **277**, 744.
Rots, A. H. 1975, *Astr. Ap.*, **45**, 43.
Rots, A. H., and Shane, W. W. 1975, *Astr. Ap.*, **45**, 25.
Sandage, A. 1984, *A.J.*, **89**, 621.
Schweizer, F. 1976, *Ap. J. Suppl.*, **31**, 313.
Segalovitz, A. 1976, *Astr. Ap.*, **52**, 167.
———. 1977, *Astr. Ap.*, **55**, 203.
Segalovitz, A., Shane, W. W., and de Bruyn, A. G. 1976, *Nature*, **264**, 222.
Shu, R. H., Milione, V., Gebel, W., Yuan, C., Goldsmith, D. W., and Roberts, W. W. 1972, *Ap. J.*, **173**, 557.
Visser, H. C. D. 1978, Ph.D. thesis, University of Groningen.
———. 1980, *Astr. Ap.*, **88**, 159.

FRANK N. BASH: Department of Astronomy, The University of Texas at Austin, Austin, TX 78712

MICHELE KAUFMAN: Department of Physics, The Ohio State University, 174 West 18th Avenue, Columbus, OH 43210